JGR Oceans

RESEARCH ARTICLE
10.1029/2024JC022032

# Benefits of a Landfast Ice Representation on Simulated Antarctic Sea Ice and Coastal Polynya Dynamics

**N. Pirlet[1], T. Fichefet[1], M. Vancoppenolle[2], A. D. Fraser[3,4], P. Mathiot[5], C. Rousset[2], A. Barthélemy[1], P.-Y. Barriat[1], C. Pelletier[6], G. Madec[2], and C. Kittel[5,7,8]**

[1]Earth and Life Institute, Earth and Climate Research Center, Université Catholique de Louvain, Louvain-la-Neuve, Belgium, [2]Sorbonne Université, CNRS, IRD, MNHN, Laboratoire d'Océanographie et du Climat: Expérimentations et Approches Numériques, LOCEAN/IPSL, Paris, France, [3]Institute for Marine and Antarctic Studies, University of Tasmania, Nipaluna/Hobart, TAS, Australia, [4]Australian Antarctic Program Partnership, Institute for Marine and Antarctic Studies, University of Tasmania, Nipaluna/Hobart, TAS, Australia, [5]CNRS/IRD/G-INP/INRAE, Institut des Geosciences de l'Environnement, Université Grenoble Alpes, Grenoble, France, [6]European Centre for Medium-Range Weather Forecasts, Bonn, Germany, [7]Département de Géographie, UR SPHERES, ULiège, Liège, Belgium, [8]Earth System Science and Department of Geography, Vrije Universiteit Brussel, Brussels, Belgium

**Abstract** The Antarctic coastal marine region is a unique and highly complex environment, of which landfast ice and polynyas are key features, especially in the context of dense water formation. Current large-scale ocean-sea ice models used in climate studies simulate hardly any Antarctic landfast ice, which has presumably negative implications on sea ice and polynya dynamics. Here we develop, implement, and evaluate an empirical circumpolar Antarctic landfast-ice representation for large-scale ocean-sea ice models. This representation is based on the restoring of sea ice velocity to zero where and when landfast ice is observed, according to a recently released circum-Antarctic landfast ice database. Using 2001–2017 hindcast simulations with the NEMO-SI$^3$ model, we demonstrate that prescribing landfast ice not only ensures accurate landfast ice coverage, as expected, but also largely improves the simulated landfast ice thickness and polynya dynamics. This includes more realistic polynya coverage, individual polynya shape, frequency, and ice production rates. Additionally, the model low bias in summer ice extent is reduced, as prescribing landfast ice locks thicker ice near the coast, taking longer to melt. Our simulations also give the first estimate of landfast ice volume, representing 10.6% of the pan-Antarctic total, compared to 3.8% of the total Antarctic sea ice extent. We argue that velocity restoring is appropriate for some investigations of the Antarctic landfast ice over the recent past, but not for the remote past or future projections, for which a physical representation of landfast ice drivers, particularly iceberg-sea ice interactions, is necessary.

**Plain Language Summary** Antarctic coastal marine regions are important for ocean dense water formation, yet challenging to represent in Earth System Models. This is particularly true for two important but complex phenomena specific to these regions: landfast ice—immobile sea ice attached to coasts or to continental ice formations—and coastal polynyas—regions of open water surrounded by sea ice, maintained by strong winds, and often found west of landfast ice. Neither landfast ice nor polynyas are well reproduced in current models, with presumably negative impacts on simulated sea ice and ocean characteristics. In this contribution, we adjust landfast ice to observations in ocean-sea ice model simulations of the Antarctic marine region and examine the impacts. We find that realistic landfast coverage improves many other aspects of the simulations, in particular polynyas, landfast ice thickness, and summer ice extent. We also quantify the volume of Antarctic landfast ice to 10.6% of the total sea ice volume, a larger fraction than for coverage (3.8%). We conclude that including landfast ice makes ocean-sea ice models more realistic in the Antarctic coastal regions. On this basis, we argue that more physical representations of landfast ice are needed, as our representation does not work out of the observed period (2001–2017).

**Key Points:**

- Prescribing Antarctic landfast ice improves realism of coastal polynyas, thickness and summer ice coverage in ice-ocean simulations
- Simulated annual mean Antarctic landfast ice volume over 2001–2017 is 10.6% of the total sea ice volume, against 3.8% for coverage
- Velocity-restoring to prescribe Antarctic landfast ice is useful for the recent past but not suitable for the distant past or the future

**Supporting Information:**

Supporting Information may be found in the online version of this article.

**Correspondence to:**

M. Vancoppenolle,
martin.vancoppenolle@locean.ipsl.fr

**Citation:**

Pirlet, N., Fichefet, T., Vancoppenolle, M., Fraser, A. D., Mathiot, P., Rousset, C., et al. (2025). Benefits of a landfast ice representation on simulated Antarctic sea ice and coastal polynya dynamics. *Journal of Geophysical Research: Oceans*, *130*, e2024JC022032. https://doi.org/10.1029/2024JC022032

Received 24 OCT 2024
Accepted 22 AUG 2025

**Author Contributions:**

**Conceptualization:** N. Pirlet, T. Fichefet, M. Vancoppenolle
**Data curation:** N. Pirlet
**Formal analysis:** N. Pirlet
**Funding acquisition:** T. Fichefet, M. Vancoppenolle
**Investigation:** N. Pirlet
**Methodology:** N. Pirlet, T. Fichefet, M. Vancoppenolle, G. Madec
**Project administration:** N. Pirlet, T. Fichefet
**Resources:** N. Pirlet, A. D. Fraser, C. Pelletier, C. Kittel
**Software:** N. Pirlet, P. Mathiot, C. Rousset, A. Barthélemy, P.-Y. Barriat



## 1. Introduction

The Antarctic coastal marine regions are a unique and highly complex environment, where multiple Earth System components meet and interact: the atmosphere, Southern Ocean waters, various forms of sea ice, ice shelves flowing from Antarctica, and the icebergs they are releasing. Some of the planet's densest oceanic water masses form on the Antarctic continental shelf (Kusahara et al., 2010, 2017; Ohshima et al., 2013, 2016, 2022), influencing the global ocean circulation and hydrography (Gordon et al., 2001; Ohshima et al., 2013; Rintoul &

**Supervision:** T. Fichefet, M. Vancoppenolle
**Visualization:** N. Pirlet
**Writing – original draft:** N. Pirlet
**Writing – review & editing:** N. Pirlet, T. Fichefet, M. Vancoppenolle, A. D. Fraser, P. Mathiot, C. Rousset, A. Barthélemy, C. Pelletier, C. Kittel

Bullister, 1999; Williams et al., 2016). Large-scale ocean-sea ice models used in climate studies have notorious difficulties to represent Antarctic coastal regions accurately, particularly in forming dense water masses at the correct location with correct properties (Heuzé, 2021).

Coastal polynyas and landfast ice are key regional features of the Antarctic coastal seascape (Massom et al., 2001). Coastal polynyas are open water regions surrounded by sea ice with an area of 10–100,000 $km^2$, maintained by strong cold winds from Antarctica, which export large amounts of new sea ice (Mohrmann et al., 2021; Morales Maqueda et al., 2004; Tamura et al., 2008) and deemed essential sites of dense water formation. Landfast ice consists of immobile sea ice anchored to coasts, continental ice, grounded icebergs, or grounded over shoals (Fraser et al., 2023). Antarctic landfast ice amounts to 3.2%–8.5% of the total Antarctic sea ice extent and exhibits pronounced seasonal variability, with a maximum in October and a minimum in early March (Fraser et al., 2021). It plays a key role in modulating coastal oceanographic processes by attenuating wave energy and altering momentum transfer (Brearley et al., 2017; Inall et al., 2022), and contributes to the mechanical stability of vulnerable ice shelves and glacier tongues (Massom et al., 2018). From a biogeochemical perspective, landfast ice acts as a seasonal reservoir of limiting nutrients, which may fertilize the coastal ocean upon ice breakup and offshore drift (Grotti et al., 2005), thereby supporting early-season primary production (Meiners et al., 2018) and sustaining marine food webs. Landfast ice also appears to influences polynya dynamics. Coastal polynyas are often found at the west side of Antarctic landfast ice tongues (Nihashi & Ohshima, 2015), suggesting that landfast ice promotes polynya by blocking westward sea ice advection (Fraser et al., 2019; Massom et al., 1998, 2001; Nihashi & Ohshima, 2015). Despite their importance, large-scale ocean-sea ice models rarely reproduce these features accurately, if at all, around Antarctica (Jeong et al., 2023; Mohrmann et al., 2021).

The limited capacity of large-scale ocean-sea ice models to simulate polynyas is often explained by the lack of strong katabatic winds in atmospheric forcing data sets (e.g., Huot et al., 2021; Mathiot et al., 2010), insufficient resolution, or missing landfast ice (Fraser et al., 2023; Jeong et al., 2023). In the Arctic, significant progress in the model representation of landfast ice has been made over the past decade (Lemieux et al., 2015, 2016; Sterlin et al., 2024). Arctic landfast ice is typically anchored to the seafloor over shallow continental shelves by large pressure ridges (stamukhi; Mahoney et al., 2014), or bottomfast via attachment to the seafloor (Dammann et al., 2019). In models, three sets of parameterizations largely improve the simulated landfast ice characteristics: first, the incorporation of a bottom friction term in the sea ice momentum equation, dependent on bathymetry and ice thickness (e.g., Dupont et al., 2022; Lemieux et al., 2015); second, the inclusion of a lateral drag in the momentum equation (Liu et al., 2022); and third, the addition of tensile strength into the classical viscous-plastic sea ice rheology (König Beatty & Holland, 2010; Lemieux et al., 2016).

However, model landfast ice parameterizations devised for use in the Arctic do not work in the Antarctic, as the landfast ice stability points differ between the two hemispheres. The Antarctic continental shelf is deeper (>200 m) than the Arctic one (vast tracts at <20 m) and landfast ice is anchored by large icebergs (Massom et al., 1998) rather than sea ice keels. Antarctic landfast ice in models could be achieved by incorporating iceberg grounding and interaction with sea ice. High-resolution regional studies show significantly improved landfast ice distribution when large icebergs are added to the land-sea mask (Huot et al., 2021; Van Achter et al., 2022). However, expanding this to circum-Antarctic scales and for long time periods remains challenging without a comprehensive database of grounded icebergs. In addition, the grounded icebergs and their interactions with sea ice are poorly understood and not yet included in large-scale models. Still, the bi-decadal, satellite-based, high-resolution, data set of the circum-Antarctic landfast ice distribution of Fraser et al. (2020) offers valuable constraints for advancing Antarctic landfast ice model representations (Fraser et al., 2023; Nihashi et al., 2023) potentially leading to improvements in the simulated dynamics of other elements, in particular coastal polynyas.

In the present study, we leverage the new landfast ice data set of Fraser et al. (2020) and question whether representing the observed Antarctic landfast ice in large-scale ocean-sea ice models simulations improves the simulated sea ice characteristics and polynya activity. To this end, we use the ocean-sea ice model NEMO-SI$^3$ (Madec et al., 2023; Vancoppenolle et al., 2023) in a regional Southern Ocean 1/4° configuration. We develop, test and evaluate an empirical, circumpolar model representation of Antarctic landfast ice: sea ice velocity is restored to zero where landfast ice is observed, according to the observational data set of Fraser et al. (2020). We then study the implications of landfast ice at circum-Antarctic scales in multi-decadal simulations of the ice-covered Southern Ocean. In particular, we examine changes in polynya activity and in large-scale sea ice

characteristics induced by the incorporation of landfast ice. The influence of landfast ice on continental shelf water properties, including dense water formation, will be explored in a forthcoming paper.

This paper is structured as follows: Section 2 describes the methods, including the ocean-sea ice model, the Antarctic landfast ice restoring algorithm, the model configuration, and the experiments conducted. Section 3 evaluates the effectiveness of the landfast ice restoring method, and its impacts on the simulated coastal polynyas and other sea ice characteristics. Finally, Sections 4 and 5 discuss the results and draw conclusions.

## 2. Materials and Methods

### 2.1. The Ocean-Sea Ice Model NEMO-SI$^3$

We use the ocean modeling system NEMO (Nucleus for European Modeling of the Ocean; Madec et al., 2023). The ocean component of NEMO represents ocean dynamics using a three-dimensional, free-surface, hydrostatic, Boussinesq approach for primitive equations, and finite-difference discretization methods. Horizontal and vertical advection of tracers are handled by fourth- and second-order flux-corrected transport schemes, respectively (Zalesak, 2012). The TEOS-10 equation of state is approximated using a polynomial function (Roquet et al., 2015). Adiabatic eddy mixing is parameterized using the Gent and Mcwilliams (1990) scheme. Internal wave mixing follows the parameterization of De Lavergne et al. (2020). A free-slip lateral boundary condition is applied to momentum, with a no-slip condition specifically implemented at the South Orkney Islands (at the northern end of the Antarctic Peninsula) as in Mathiot and Jourdain (2023). This local adjustment aims to account for the influence of complex sub-gridscale bathymetry on water mass properties. Other modeling choices, including momentum advection, lateral diffusion of momentum and tracers, vertical mixing, convection, double diffusion, and bottom boundary layer treatment are set according to Storkey et al. (2018).

As a sea ice component, we use SI$^3$ (Sea Ice modeling Integrated Initiative), a dynamic-thermodynamic continuum sea ice model (Rousset et al., 2015; Vancoppenolle et al., 2023), directly resolved on the NEMO ocean grid. SI$^3$ features an energy- and salt-conserving approach for sea ice thermodynamics (Vancoppenolle et al., 2009), multiple categories to resolve subgrid-scale variations in ice thickness (Bitz et al., 2001; Lipscomb, 2001), a second-order-moment-conserving scheme for horizontal advection (Prather, 1986), and the adaptive elastic-viscous-plastic (aEVP) formulation for the rheology term of the momentum equation (Kimmritz et al., 2016).

Here we use NEMO version 4.2.0 which has been corrected for an important bug found in the calculation of the ice-ocean stress, resolved in version 4.2.2.

### 2.2. An Observation-Based Representation of Antarctic Landfast Ice

Since the physically based representation of iceberg-sea ice interactions at the circumpolar scale exceeds current understanding and model capabilities, we propose an observation-based approach: immobilizing the simulated sea ice where and when landfast ice is observed, using the landfast ice observational data set of Fraser et al. (2020). This approach involves three components: an observation-based landfast ice mask, a restoring term that sets sea ice velocity close to zero, and switching off new ice formation in open water within the landfast ice zone once sea ice concentration reaches its maximum, to prevent excessively rapid sea ice thickening. Throughout this paper, when we refer to *prescribing landfast ice*, we specifically mean these three components.

The first element of the landfast ice representation is the observation-based, time-dependent mask that informs on the presence of landfast ice in each model grid cell (Figure 1). To construct this mask, we start from the satellite-based, 1 km-resolution, bi-weekly data set of landfast ice presence produced by Fraser et al. (2020), which covers the complete years from 2001 to 2017. This data set is linearly upscaled in time and downscaled in space to produce a daily landfast ice presence mask at the model resolution (roughly 10 km close to the Antarctic coastline). We found it convenient to spatially threshold the mask to 0 for concentrations below 50% (no landfast ice) and 1 for concentrations of 50% or higher (full coverage).

The second element is a restoring scheme for sea ice velocity, to damp the simulated sea ice velocity components to practically zero where and when landfast ice is observed, without directly impacting the velocities elsewhere. The restoring applies at each sub-time step of the aEVP scheme, with a restoring strength parameter $\tau$ (see Appendix A). After testing, we found that $\tau = 0.01$ ensures numerical stability and convergence within 120

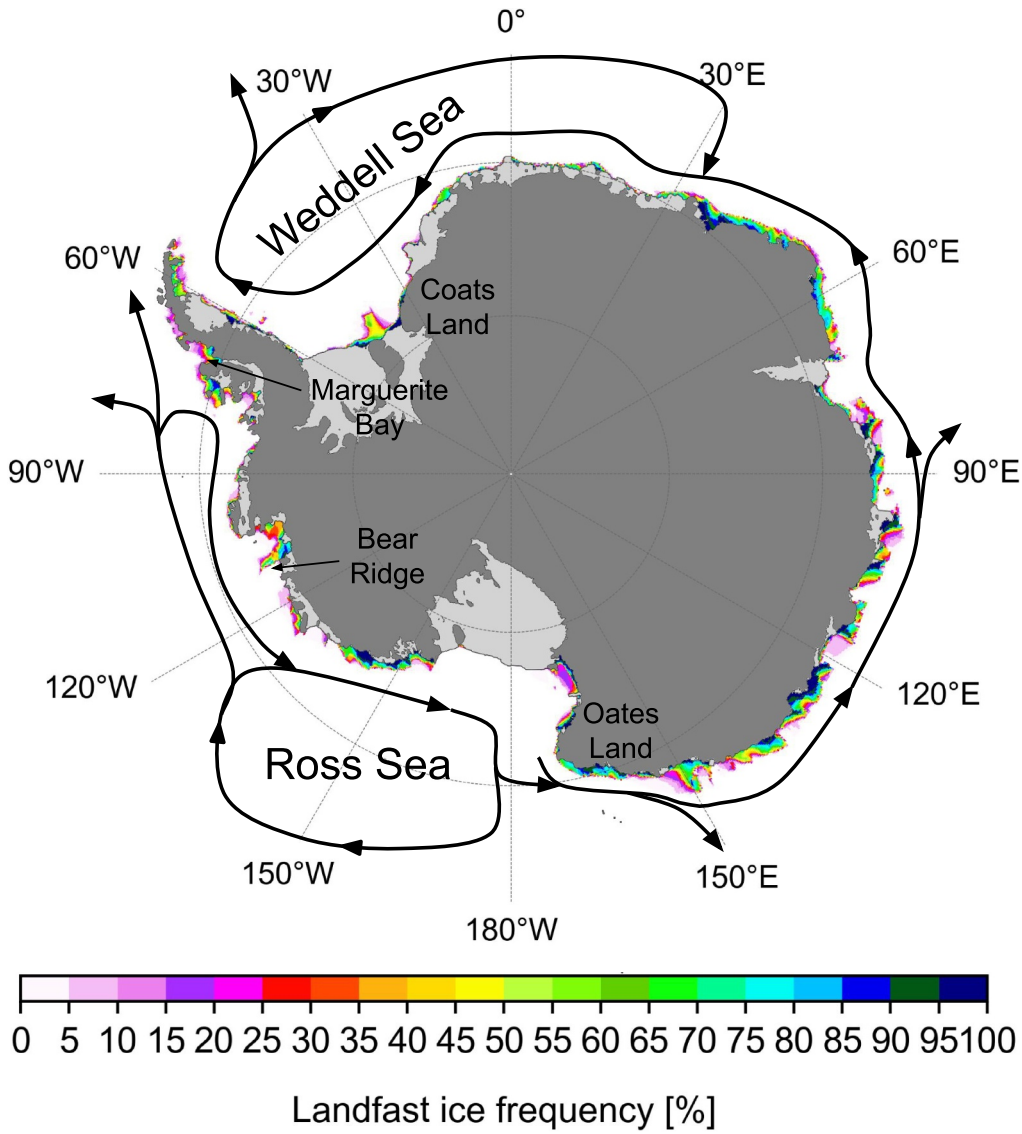


**Figure 1.** Annual frequency of occurrence of landfast ice averaged over the period 2001–2017 as derived from the Fraser et al. (2020) data set and interpolated on the model grid. Black arrows show the pathway of the simulated surface coastal oceanic currents and connected gyres. Some important locations mentioned in the text are indicated in the figure.

subcycle iterations. The landfast ice mask is also applied to strain rate tensor invariants (tension, shear, and divergence) used as intermediate steps in the dynamics solver, and also as input for mechanical redistribution of sea ice.

The third and last element of our landfast ice representation is to preclude new ice growth in open water in compact landfast ice conditions. By default, a minimum fraction of open water (here 5%) is imposed, to compensate for insufficient opening by ice dynamics and ensure enough air-sea heat exchange. By allowing a minimum level of new ice growth in open water, this significantly impacts the Antarctic sea ice mass balance also to ocean surface buoyancy forcing at large-scales. However, preliminary tests have indicated that allowing ice growth in open water in the landfast ice zone exposes coastal waters to cold air from Antarctica, inducing excessive sea ice growth, leading rapidly to ice up to 20 m in thickness in some landfast ice regions. Such values for landfast ice tongues are unrealistic, as Antarctic landfast ice thickness typically ranges from 1 to 3 m for seasonal ice and up to 5 m for deformed multiyear ice (Nakamura et al., 2009), with extreme cases reaching 50 m (Massom & Stammerjohn, 2010). To circumvent this issue, we preclude air-sea exchanges and ice formation in

open water when open water fraction is 1% above the minimum threshold and velocity is lower than 0.0005 m $s^{-1}$, which corresponds to compact landfast ice conditions.

### 2.3. The eANT025 Configuration

As we focus on Antarctic landfast ice, we developed the eANT025 configuration derived from the eORCA025 configuration (Mathiot & Jourdain, 2023). This configuration includes the sea ice region, the Southern Ocean, the Antarctic ice shelves and a single boundary at 30°S. The nominal resolution is 0.25° (less than 12 km grid spacing at 65°S). The eANT025 grid is quasi-isotropic and includes an accurate representation of under-ice shelf cavities (Mathiot et al., 2017). All Antarctic ice shelf cavities are encompassed by the model grid. Basal melt rates in ice shelf cavities are calculated following Mathiot et al. (2017), with parameter values from Mathiot and Jourdain (2023). Vertical discretization comprises 121 levels, with a nonlinear increase in vertical level thickness, from 1 m at the surface to around 20 m from 100 to 1,000 m depths, and up to 200 m near the ocean bottom. Partial steps (Barnier et al., 2006) are used to represent as closely as possible the actual bathymetry and the ice shelf draft. The bathymetry and ice shelf draft are the same as those employed by Mathiot and Jourdain (2023). We omitted the line of icebergs grounded on Bear Ridge (110°W, 74°S) introduced by Mathiot and Jourdain (2023), as we found that prescribing landfast ice brings essentially the same benefits on Amundsen sea ice and water masses as those of the iceberg line (described in Bett et al. (2020)).

At the domain lateral boundary (30°S), a flow relaxation scheme (Engedahl, 1995) is applied for the three-dimensional ocean variables, whereas a Flather scheme (Flather, 1994) is utilized for barotropic velocities and sea surface elevation. The lateral boundary conditions are derived from the Ocean Reanalysis System 5 (ORAS5) data (Zuo et al., 2019), which are interpolated over the 121 model levels.

Default $SI^3$ settings provided in the NEMO distribution (Rousset et al., 2015; Vancoppenolle et al., 2023) are used, with the following exceptions. Five subgrid-scale ice thickness categories and two vertical ice layers are employed. Drag coefficients of $5.0 \times 10^{-3}$ and $1.4 \times 10^{-3}$ are used to calculate ice-ocean and ice-atmosphere stresses, respectively. The ice strength thickness parameter $P^*$ is set to $1.5 \times 10^4$ N $m^{-1}$. Snow thermal conductivity is 0.35 W $m^{-1}$ $K^{-1}$ and the minimum open water fraction is 5%, as in Boucher et al. (2020); Mathiot and Jourdain (2023).

The surface boundary conditions are computed from the fifth generation ECMWF atmospheric reanalysis (ERA5, Hersbach et al., 2020) through the CORE bulk formulas (Griffies et al., 2009; Large & Yeager, 2004). Three-hourly data including temperature, wind velocity components, humidity, radiative fluxes (shortwave and long wave), precipitation (solid and liquid), and sea level pressure are used. Because of the importance of coastal winds in polynya formation, ERA5 is the preferred choice (Caton Harrison et al., 2022).

Coastal snow depth poses a challenge, particularly along the coasts of Antarctica where snowfall in ERA5 can reach up to a few meters per year. NEMO-$SI^3$ has no physical representation of blowing snow, hence where snowfall is high, snow accumulates locally, forming snow ice (Fichefet & Maqueda, 1999). This leads to sea ice of up to 30 m in thickness after a few years of simulation in several coastal regions, particularly in Marguerite Bay (see Figure 1), where multi-year landfast ice is observed. Very thick landfast ice is not unrealistic (Massom et al., 2001). However with default model settings and raw precipitation fields, this process occurs over excessively large areas. Ultimately, this poses problems for the ocean as unlimited ice formation leads to large local salt accumulation in the upper waters, which the ocean model component badly deals with. Therefore to address this, we corrected solid precipitation. The input solid precipitation field was rescaled where the 1979–2017 average annual snow accumulation exceeds 2.75 m of snow. This threshold was adjusted to avoid ice thickness to reach more than about 20 m in the most extreme cases. Practically, the 3-hourly snowfall precipitation field is multiplied by 2.75 m, and divided by the 1979–2017 local mean snowfall accumulation. Note that capping precipitation was also adopted by Wongpan et al. (2024).

### 2.4. Experimental Design

We ran a series of simulations illustrated in Figure 2, designed to highlight the impacts of Antarctic landfast ice. A 1979–2001 spin-up simulation (INIT) was designed to produce initial ocean and sea ice conditions for the other simulations. This spin-up was itself initialized from rest using ocean temperatures and salinities from the WOA2018 climatology (World Ocean Atlas 2018, Locarnini et al., 2018; Zweng et al., 2019), and sea ice

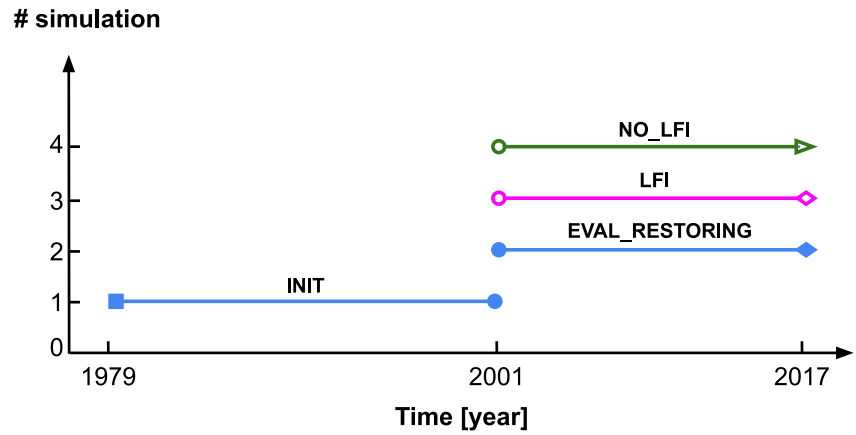


**Figure 2.** Name and length of the simulations carried out in the study.

concentration and thickness fields from a 1980–2004 global simulation (GO6, Storkey et al., 2018). The spin-up did not include landfast ice restoring.

Then three experiments were run over the time period 2001–2017. The two main simulations used in this paper are the LFI (for LandFast Ice) and NO_LFI (for No LandFast Ice) simulations, which have the landfast ice representation on and off, respectively. By comparing LFI to NO_LFI, the impact of Antarctic landfast ice can be isolated. In these simulations, salinity restoring is off and a freshwater flux correction diagnosed from EVAL_RESTORING is applied as an external climatological monthly freshwater flux, which avoids interference with the signal of interest. EVAL_RESTORING includes prescribed landfast and salinity restoring toward the World Ocean Atlas climatology (WOA2018; Zweng et al., 2019), and per se implicitly incorporates the effects of iceberg melting and coastal runoff. However, in our model configuration, this correction is disabled near the Antarctic coast to avoid interference with polynyas, which can result in a freshwater bias in this region. Nonetheless, this bias should be small, as runoff from the Antarctic ice sheet and iceberg melt close to the coast are very weak (Ackermann et al., 2024; Kittel et al., 2021). It is worth stressing that the freshwater flux from the Antarctic ice shelves is explicitly simulated by the model.

Landfast ice and polynyas were diagnosed from outputs for NO_LFI and LFI simulations. Daily landfast ice presence was derived from daily sea ice velocity output, assuming sea ice is landfast when velocity is below $5 \times 10^{-4}$ m s$^{-1}$, following Lemieux et al. (2016), and then converted into annual and climatological frequency maps. Landfast ice extent is defined as the extent where sea ice is landfast and its concentration exceeds 15%. Polynya presence was diagnosed by applying a polynya-detection algorithm that identifies connected open water coastal regions where daily grid-cell mean ice thickness is below a 25 cm threshold (see Appendix B). This threshold is within the 10–30 cm range used in previous works (Jeong et al., 2023; Mohrmann et al., 2021; Nihashi & Ohshima, 2015; Ohshima et al., 2016; Tamura et al., 2006, 2008). Analyses were repeated for thresholds of 20 and 30 cm, and provided as Table S1 in Supporting Information S1 and suggest that the results remain robust across this reasonable range of thresholds. Daily polynya presence was converted into cold-season (March–October) polynya frequency. Following Tamura et al. (2016) and Nihashi and Ohshima (2015), we consider 13 major Antarctic coastal polynyas (see Section 3.2.1).

### 2.5. Observational Products Used for Model Evaluation

Several observational products were used to evaluate the simulated sea ice, landfast ice, and polynya dynamics. First, we use the 2001–2018 circum-Antarctic landfast ice distribution data set (Fraser et al., 2020), based on visible and thermal infrared imagery from MODIS. This data set has a spatial resolution of 1 km and a temporal resolution of 15 days.

By comparison with coverage, landfast ice thickness observations are sparse. With no well-validated satellite thickness product available in the landfast ice region, we instead utilized in situ data from the Antarctic Fast Ice Algal Chlorophyll-a (AFIAC) database (Meiners et al., 2018), which compiles 888 geo-referenced ice cores collected between 1970 and 2015 near manned Antarctic coastal stations. Among the nine sampling stations, six

**Table 1**
*Seasonal Minima, Mean and Maxima of Ice Extent and Volume for the LFI and NO_LFI Simulations, for Landfast Ice-Only and Pan-Antarctic Sea Ice Zone Domains, Over 2001–2017*

| | | Extent $[10^6 km^2]$ | | Volume $[10^3 km^3]$ | |
|---|---|---|---|---|---|
| Sea ice region | Time in the year | LFI | NO_LFI | LFI | NO_LFI |
| Landfast ice | @Minimum | 0.22 ± 0.04 | 0.02 ± 0.01 | 0.69 ± 0.13 | 0.1 ± 0.04 |
| | @Mean | 0.47 ± 0.03 | 0.04 ± 0.01 | 1.21 ± 0.1 | 0.17 ± 0.04 |
| | @Maximum | 0.64 ± 0.05 | 0.07 ± 0.01 | 1.73 ± 0.13 | 0.26 ± 0.07 |
| Pan-Antarctic | @Minimum | 1.63 ± 0.38 | 1.6 ± 0.39 | 2.68 ± 0.45 | 2.16 ± 0.42 |
| | @Mean | 12.24 ± 0.43 | 12.31 ± 0.44 | 11.43 ± 0.72 | 10.9 ± 0.71 |
| | @Maximum | 19.45 ± 0.46 | 19.51 ± 0.47 | 21.41 ± 0.93 | 20.94 ± 0.94 |

were retained based on data coverage: Syowa, Davis, Dumont D'Urville, McMurdo, Rothera, and Neumayer. For comparison with the model output, simulated landfast ice data are averaged within a 5 × 5 grid cell box centered on the station coordinates.

Finally, the coastal polynya distribution from Nihashi and Ohshima (2015) is used to evaluate the spatial distribution of the simulated polynyas. Polynya presence is based on thin ice thickness retrieval algorithms applied to AMSR-E passive microwave signals, and data cover March to October, over 2003–2011. This product uses the National Snow and Ice Data Center (NSIDC) polar stereographic grid, which has a grid resolution of approximately 6.25 km.

For comparison, both landfast ice and polynya products were interpolated onto the ∼10 km model grid.

## 3. Results

### 3.1. Landfast Ice Characteristics

We first analyze the characteristics of the simulated landfast ice in the LFI and NO_LFI simulations against available observations.

#### 3.1.1. Quality Control of the Landfast Ice Extent

If it functions as intended, velocity restoring in LFI should promote the formation of landfast ice where and when it is observed. This method acts solely on sea ice velocities by restoring them toward zero in predefined coastal regions; it does not explicitly prescribe the presence of landfast ice. Consequently, perfect agreement with observed landfast ice extent is not guaranteed: (a) if no sea ice is present, there is no sea ice velocity to restore, and (b) some landfast ice may still form in the absence of restoring.

In particular, landfast ice extent and its seasonal (see Table 1) and inter-annual variations (see Figure 3a) are closely reproduced in LFI and not captured in NO_LFI. Landfast ice extent in LFI needs one spin-up season of ice growth to adjust to observations, reconstructed from Fraser et al. (2020); Fraser et al. (2021); and from then on features the large seasonal cycle between the summer minimum (∼2 × $10^5$ $km^2$, reached in March) to maximum (∼6-8 × $10^5$ $km^2$, reached in September). By contrast, the landfast ice extent in NO_LFI is much smaller than observed (<$10^5$ $km^2$) and has a weaker seasonal cycle. The quality of the model-observation agreement is seasonal: the maximum landfast ice extent simulated in LFI is closer to the observational value than the minimum, presumably because of excessive summer melting, which has already been seen using earlier versions of NEMO-SI$^3$ (Barthélemy et al., 2018; Rousset et al., 2015; Van Achter et al., 2022; Vancoppenolle et al., 2009).

Spatially speaking, landfast ice is also simulated at correct positions and times in the LFI simulation. Indeed, differences of annual frequency of occurrence of landfast ice averaged over years 2001–2017 between the mask and the LFI simulation remains generally low (Figure 4), with most regions showing differences within ±5%. However, localized discrepancies exceeding ±20% of frequency of occurrence are observed. Delimited by Coats Land (20°W) and Oates Land (170°E), two distinct trends emerge: the eastern sector shows a lower simulated frequency of occurrence of landfast ice, whereas the western sector exhibits a higher. The indented coastline of the

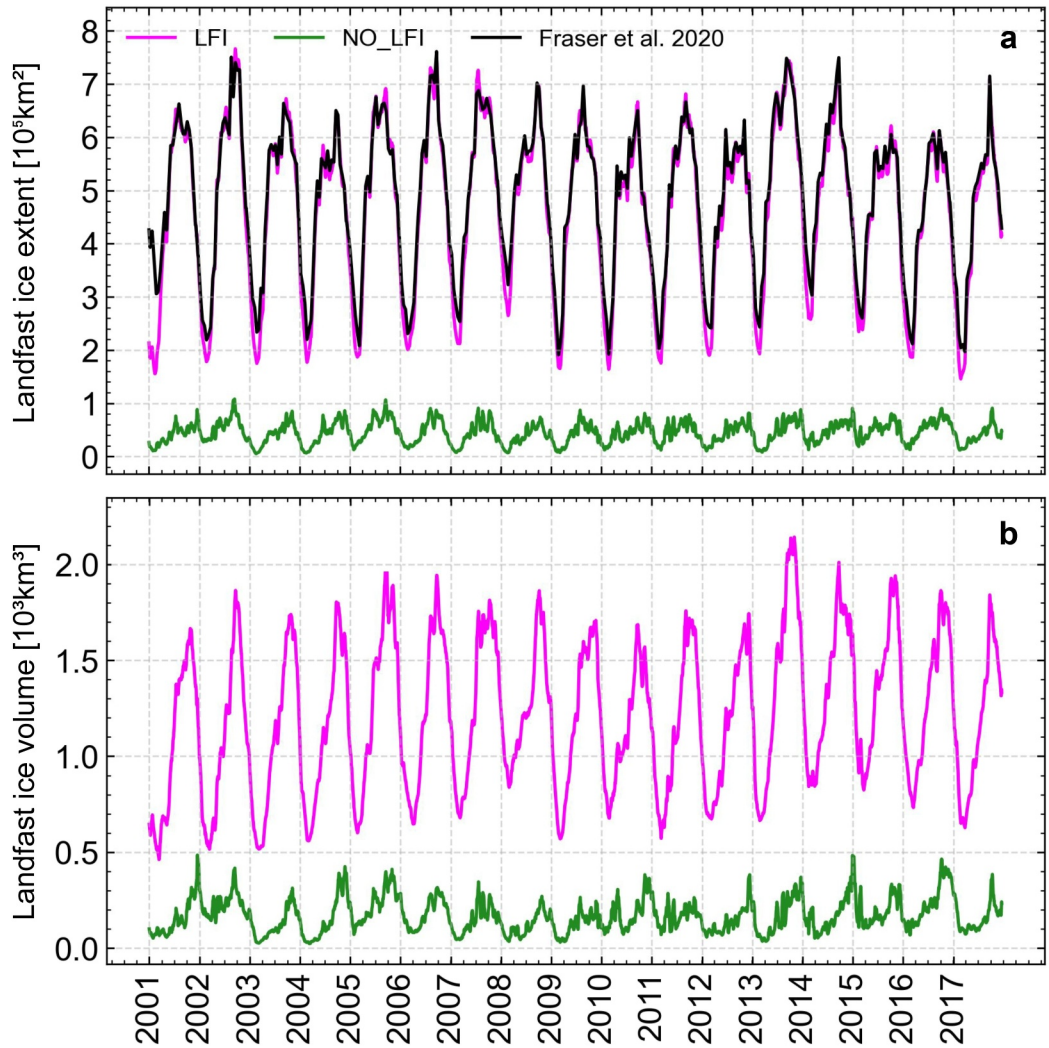


**Figure 3.** Fifteen-day moving average of daily landfast ice extent (a) and volume (b) over the period 2001–2017 for both the LFI and NO_LFI simulations. Panel (a) used here as a quality control step, also includes observed landfast ice extent from Fraser et al. (2020).

West Antarctica and the Antarctic Peninsula compared to the smoother coastline of East Antarctica can explain trends of opposite sign. Figure 4 shows that all major landfast ice regions seen in observations are reproduced in the LFI simulation. A few narrow bays (totaling ~6% of annual mean landfast ice extent) have near-100% occurrence frequency (main Figure 5), which indicates multi-year landfast ice is simulated.

### 3.1.2. Landfast Ice Thickness and Volume

Landfast ice thickness is also better captured in the LFI simulation than in the NO_LFI one. To assess this, the simulation output was compared to in situ ice thickness observations from an ice core database (Figure 5). We do not expect an exact model-observation match because the comparison is inconsistent in terms of spatial and temporal scales. The model output is taken from several neighboring grid cells (5 × 5 box), whereas observations come from a single location. In addition, observational records come from different years and we compare them to multi-year averages from simulation output. Nevertheless, we find that in four out of six sites retained for analysis (Neumayer, McMurdo, Davis, Dumont d'Urville), the LFI simulation better reproduces the observed seasonal development of ice thickness than the NO_LFI one. Specifically, LFI simulates a seasonal thickness maximum above 1 m, which is much closer to observations than the seasonal maximum thickness in NO_LFI, which remains below 50 cm. At these sites, there is no landfast ice in NO_LFI, whereas some is present in LFI—this highlights

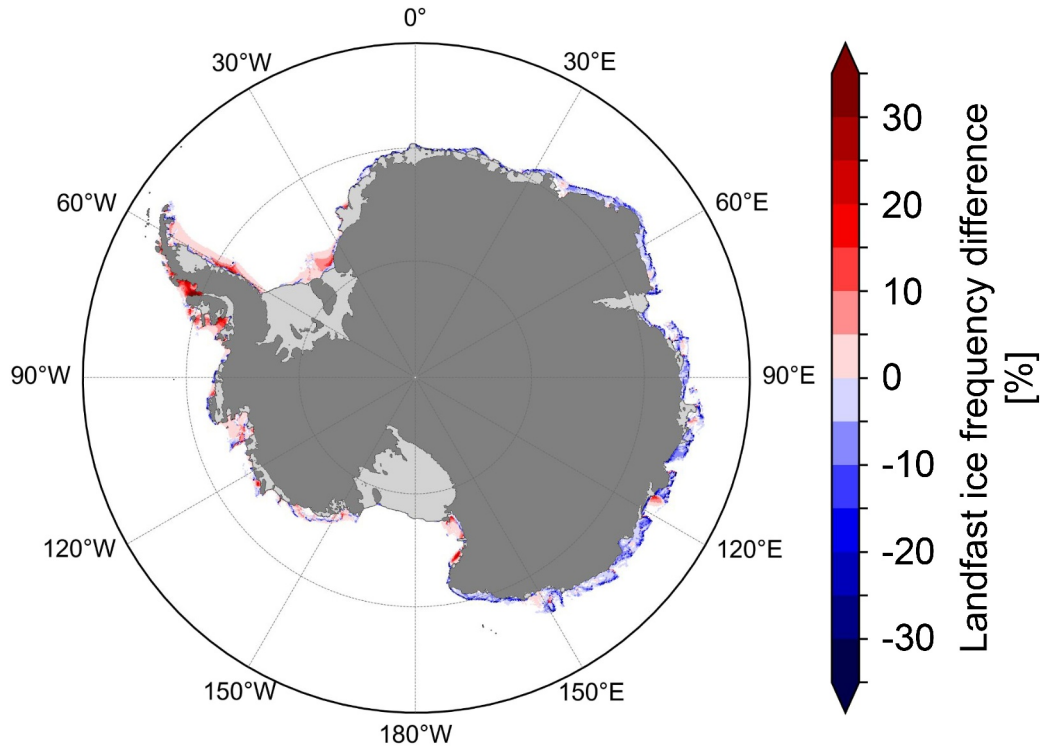


**Figure 4.** Difference of annual frequency of occurrence of landfast ice between the LFI simulation and the Fraser et al. (2020) data set averaged over years 2001–2017. Red shading indicates regions where landfast ice is simulated more frequently than observed, whereas blue shading marks regions where it is simulated less frequently than observed.

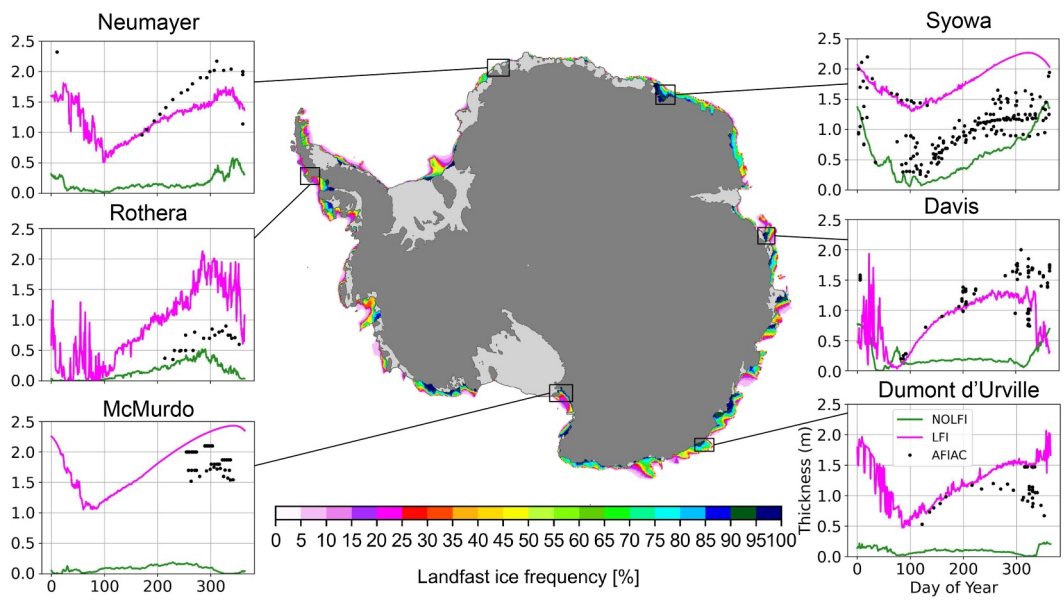


**Figure 5.** Main figure: Annual frequency of occurrence of landfast ice averaged over years 2001–2017 as simulated in LFI. Sub-figures: Sea ice thickness from cores associated with six research stations (black dots; from Meiners et al. (2018)), and the daily 2001–2017 mean seasonal cycle of landfast ice (sea ice with a velocity lower than 0.0005 m $s^{-1}$) thickness for both simulations (pink = LFI, green = NO_LFI).

**Table 2**
*Annual Sea Ice Production (Mean ± Standard Deviation, 2001–2017) Over the Sea Ice Production Season (March–October) for the 13 Major Coastal Polynya Regions*

| Sea ice production ($\times 10$ km$^3$ yr$^{-1}$) | Literature range | LFI | NO_LFI | Δ (LFI-NO_LFI) |
|---|---|---|---|---|
| Cape Darnley (CDP) | 13.8–18.4 | 10.5 ± 0.7 | 8.9 ± 0.5 | 1.6 [+18%] |
| Mackenzie Bay (MBP) | 6–9.8 | 9 ± 0.8 | 9.3 ± 0.8 | −0.3 [−3%] |
| Barrier (BaP) | 6.2–10.1 | 7 ± 0.9 | 4 ± 0.4 | 3 [+75%] |
| Shackleton (SP) | 8.4–12.3 | 12 ± 1.6 | 8.5 ± 1 | 3.5 [+41.2%] |
| Vincennes Bay (VBP) | 6.4–9 | 9.7 ± 1.3 | 5.5 ± 0.9 | 4.2 [+76.4%] |
| Dalton (DaP) | 3.5–5.1 | 4.1 ± 0.5 | 1.2 ± 0.2 | 2.9 [+241.7%] |
| Dibble (DiP) | 5.7–8.5 | 5.7 ± 0.6 | 2.3 ± 0.2 | 3.4 [+147.8%] |
| Mertz (MP) | 13.2–17.2 | 16.1 ± 3.2 | 11.6 ± 1 | 4.5 [+38.8%] |
| Terra Nova Bay (TNBP) | 5.5–6.6 | 3.4 ± 0.3 | 3.1 ± 0.2 | 0.3 [+10%] |
| Ross Ice Shelf (RISP) | 30–38.2 | 29.9 ± 2 | 30.3 ± 1.8 | −0.4 [−1%] |
| Amundsen (AP) | 9–12.3 | 5.6 ± 1.3 | 3.1 ± 0.6 | 2.5 [+80.6%] |
| Bellingshausen (BeP) | 2.6–8.1 | 3.9 ± 0.7 | 3.9 ± 0.6 | 0 [0%] |
| Ronne Ice Shelf (RONP) | 3.8–7.1 | 7.2 ± 0.9 | 7.1 ± 0.9 | 0.1 [+1%] |
| Total | 117–150.8 | 124.1 ± 5.6 | 98.7 ± 3.2 | 25.4 [+25.7%] |

*Note.* Sea ice production is calculated for grid cells where the 2001–2017 mean polynya frequency is higher than 25%. The last column represents the LFI minus NO_LFI sea ice production difference and relative difference in brackets. The literature range combines satellite-based products of the following studies: Nihashi and Ohshima (2015), Tamura et al. (2016), Nakata et al. (2021).

how the locking of landfast ice in LFI allows for seasonal thickening. In NO_LFI, by contrast, the sea ice is not locked, and the thinning effects of import and export are presumably overestimated. The two other sites (Rothera and Syowa) already feature landfast ice in NO_LFI (probably because these sites are enclosed within narrow bays prone to lock the ice), and therefore no improvement in thickness can be seen in the LFI simulation. The long-term mean Antarctic landfast ice thickness over 2001–2017 is ∼2.9 m, consistent with the fast ice thickness distribution data from the West Ross Sea reported by Langhorne et al. (2023).

Our simulations also inform on the simulated Antarctic landfast ice volume (see time series in Figure 3b and statistics in Table 1), which benefits from close-to-observed landfast ice extent and improved ice thickness in LFI. The long-term annual mean landfast ice volume simulated in LFI is 1,210 km$^3$, which represents 10.6% of the pan-Antarctic total sea ice volume, that is, more than the contribution of landfast ice to ice extent (3.8%). In addition, the landfast ice volume in LFI is much larger than the 170 km$^3$ simulated in NO_LFI, due to a significantly larger landfast ice extent. The simulated landfast ice volume in LFI is highly seasonal, but less than extent: the landfast ice volume increases by 2.5 on average between minimum (March) and maximum (October), and by 2.9 for extent. Moreover, the maximum volume is reached 1 month later than the maximum extent.

### 3.2. Impacts of Prescribing Landfast Ice

We have seen that the velocity restoring technique allows us to constrain the landfast ice coverage and thickness. Now, we analyze the impacts on coastal polynyas and large-scale sea ice characteristics.

#### 3.2.1. Simulated Coastal Polynyas

Does landfast ice improve the realism of the simulated coastal polynyas? To address this question, we analyzed 13 polynya regions separately following the decomposition of Nihashi and Ohshima (2015), also used in Tamura et al. (2016) and Nakata et al. (2021). Acronyms for each of the regions are given in Table 2. For each region, we mapped the average 2001–2017 polynya frequency (see Figure 6), and we also evaluated the polynya area (Table S2 in Supporting Information S1) and annual sea ice production (Table 2).

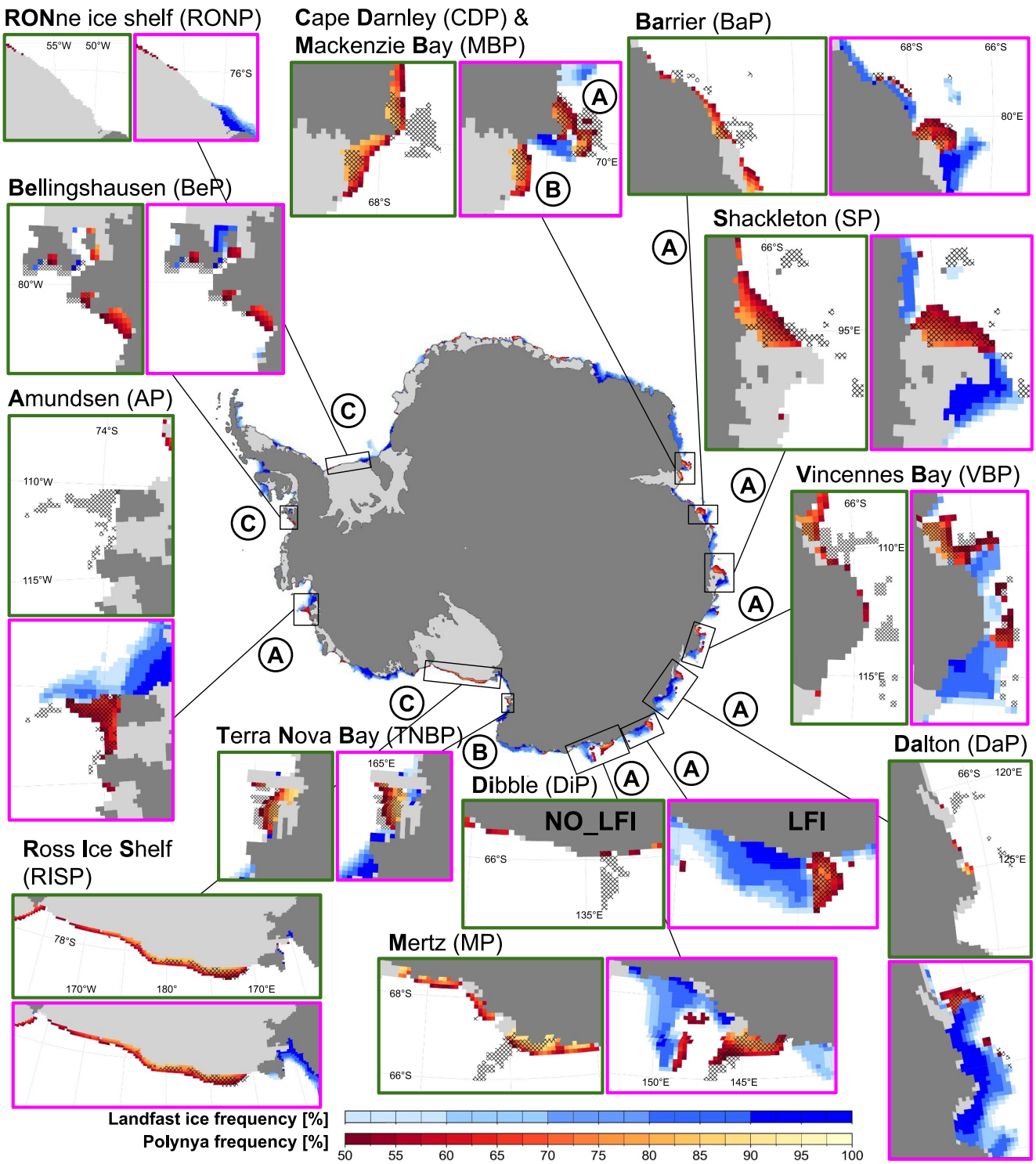


**Figure 6.** Simulated frequency of occurrence of coastal polynyas (red shading) and landfast ice (blue shading) frequency of occurrence, averaged from March to October over the period 2001–2017, in NO_LFI (green) and LFI (pink), for the 13 major coastal polynya regions. Hatched cells indicate the satellite-based polynyas as reported from an independent study (Nihashi & Ohshima, 2015). Letters indicate: (a) landfast ice is essential in polynya formation, (b) landfast ice only impacts the shape of the polynya, and (c) landfast ice does not impact the polynya.

First we examine the location, shape, and area of coastal polynyas in each individual regions. The NO_LFI simulation (green frames in Figure 6) produces realistic polynya location and shape for only 3 out of 13 regions: RONP, RISP and BeP. This is expected as these polynyas are not associated with landfast ice (see Massom et al., 1998). In contrast, the LFI simulation (pink frames in Figure 6) generates reasonable shape and location for all 13 polynya regions. More precisely, six polynyas (DiP, DaP, AP, VBP, MP, and BaP) are too small or even missing in NO_LFI and properly developed in LFI. For these, from the NO_LFI to the LFI simulations, the polynya area increases by +88.1%, +96.4%, +96.4%, +35.6%, +58.6%, and +47.4% of the LFI mean, respectively. In those six regions, landfast ice can therefore be considered essential for polynya development. Four polynyas (SP, CDP, MBP, and TNBP) do not drastically change in size but have much more realistic shape in the LFI simulation: SP area does not change and CDP slightly expand (+4.8%), whereas the size of MBP and TNBP decreases (−40.1% and −7.7%, respectively).

The total polynya area summed over the 13 regions is 79,400 ± 9,600 $km^2$ in LFI, which is about 24,300 $km^2$ lower than the lower boundary of the observational range (103,700–124,900 $km^2$, Tamura et al., 2016; Nakata et al., 2021). Uncertainties in total polynya area due to the thickness threshold used for polynya detection are significant, though. We found a difference of 25,200 $km^2$ (31%) in total polynya area for a 5 cm change in the thickness threshold value, which is in line with uncertainties in observation-based products (see Nakata et al., 2021). This large sensitivity of the polynya area to definition has been noted in previous works (e.g., Mohrmann et al., 2021). In NO_LFI, the total polynya area is 52,200 ± 3,600 $km^2$, which is >50,000 $km^2$ lower than the lower boundary of the observational range. Therefore, when landfast ice is imposed in LFI, the total polynya area increases by 52% of the NO_LFI mean.

The total annual ice production summed over the 13 polynyas is comparatively less affected by the thickness threshold used for polynya detection than the total area: total ice production in polynyas is ∼200 $km^3$ (15%) for a 5 cm change in threshold thickness. Total ice production is 1,241 ± 56 $km^3$ $yr^{-1}$ in LFI, which is compatible with literature-based estimates (1,170–1,508 $km^3$ $yr^{-1}$, mostly from observation-based retrievals) in the LFI simulation. In contrast, the NO_LFI simulation (987 ± 32 $km^3$ $yr^{-1}$, see Table 2) is below the literature range. Landfast sea ice increases annual sea ice production in polynyas by 254 $km^3$, that is, 26% of the NO_LFI mean.

Moreover, in the LFI simulation, the annual sea ice production falls within the literature range for 10 polynya regions (against 5, out of 13, in the NO_LFI simulation). The last column of Table 2 shows the change in sea ice production for each polynya from NO_LFI to LFI. In the eight polynyas, annual ice production increases by 16–45 $km^3$, or 18%–40%, from NO_LFI to LFI. For the five other polynyas, the annual sea ice production changes very little. This includes the three polynyas that are well reproduced in NO_LFI (RONP, RISP, and BeP) and two polynyas (TNBP and MBP) with significant shape changes but weak changes in ice area. Negative changes in sea ice production are not significant, as they remain below 3%.

It must be noted that the annual ice production over the entire continental shelf (water depth <1,200 m) remains nearly unchanged between LFI and NO_LFI, with a difference of only −46 $km^3$ (0.5%) out of approximately 7,800 $km^3$ $yr^{-1}$. To investigate why, we divided the continental shelf into three regions based on landfast ice and polynya activity in the LFI simulation. The LANDFAST region includes grid cells with >50% landfast ice frequency, the POLYNYA region consists of cells with >25% polynya frequency, and the ELSE region encompasses the remainder of the continental shelf. From NO_LFI to LFI, the annual ice production decreases by 836 $km^3$ in the LANDFAST region, whereas it increases by 362 $km^3$ in the POLYNYA region and by 428 $km^3$ in the ELSE region. The decrease in the LANDFAST region can be attributed to two factors: first, new ice formation in open water is forced to zero within the landfast ice mask in the LFI simulation; second, part of this region consists of relatively thin ice or polynyas in the NO_LFI simulation, producing significantly more new ice than the thicker landfast ice in LFI. The increase in annual ice production in the POLYNYA region occurs because it features active polynyas in LFI compared to thicker ice in NO_LFI. The increase in the ELSE region results from remote effects: wider, more active polynyas in the LFI simulation export thin ice, leading to overall thinner, more productive ice on the continental shelf. In summary, realistic landfast ice in LFI redistributes ice production on the continental shelf compared to NO_LFI, with decreased production under landfast ice almost offset by increases elsewhere.

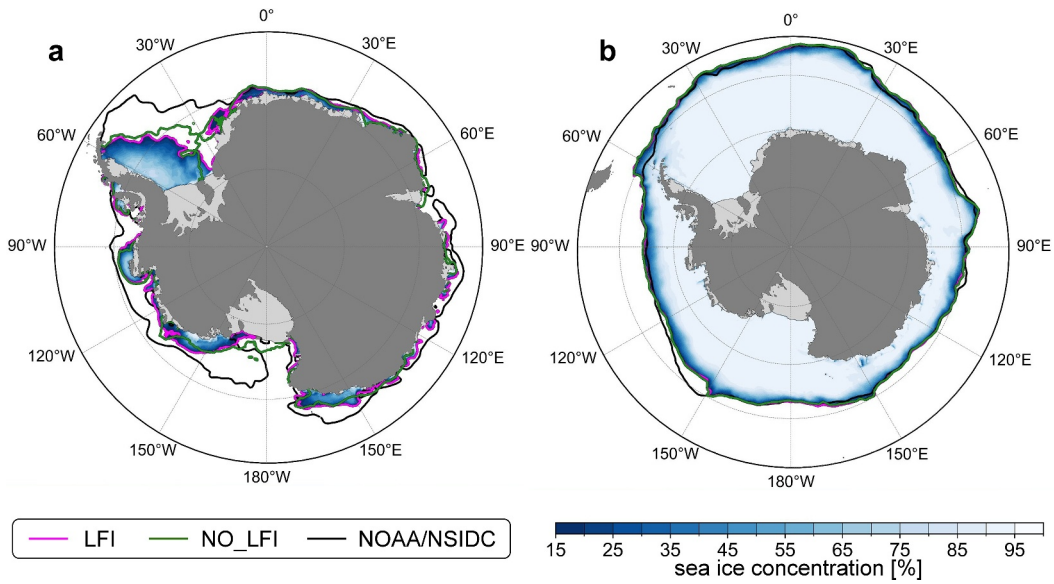


**Figure 7.** (a) February and (b) September sea ice concentration (2001–2017 average) in the LFI simulation (shading); and 15% sea ice concentration contours from the LFI (solid pink) and NO_LFI (solid green) simulations, as well as from an observational product (solid black), the NOAA/NSIDC Climate Data Record of Passive Microwave 12.5 km Sea Ice Concentration, Version 5 (black).

### 3.2.2. Impacts on Large-Scale Sea Ice Characteristics

Does landfast ice affect other large-scale sea ice characteristics (concentration, thickness)? Overall, landfast ice has a very limited impact on the Antarctic sea ice extent (<0.5% change, see Table 1), at the time of winter maximum (Figure 7b), when landfast ice is far from the ice edge, and the atmospheric forcing and simulated Antarctic Circumpolar Current largely constrain the ice edge location. In summer, however, sea ice coverage increases in some regions in the LFI simulation compared to the NO_LFI one, mitigating the summer ice extent bias (see Section 3.1.1). This is particularly the case along the coasts of East Antarctica (65°−180°E), where in February, the ice coverage increases by 65,000 km$^2$, or ∼20% (Figure 7a). Indeed, prescribing landfast ice in LFI locks some patches of thick multi-year landfast ice along the east Antarctic coasts (see pink vs. green curves in Figure 7a). These patches take a longer time to melt, which ultimately mitigates the bias of too low sea ice extent (Lin et al., 2023).

Landfast ice also largely affects the simulated sea ice thickness, in particular in the vicinity of the coasts. Overall, sea ice is 6.7% thicker in the LFI simulation than in the NO_LFI simulation, whereas its extent remains nearly unchanged (see Table 1). This highlights the impact of landfast ice on the total sea ice volume. However, regionally, thickness changes can be positive or negative and present a rather complex spatial structure (see Figure 8). Within the landfast ice velocity restoring mask, locking landfast ice prevents sea ice export and gives the ice more time to thicken (see Figures 8c and 8d). Thicker sea ice is also observed upstream of the landfast ice mask (see Figure 1). There, the direction of the sea ice drift (Figures 8c and 8d) suggests that landfast ice can block sea ice, leading to still ice that thickens thermodynamically. A similar process, leading to thick ice upstream of landfast ice, was observed by Langhorne et al. (2023). However, still ice, although motionless, is not attached like landfast ice, and can therefore be exported by strong winds. During such release events of thick ice, offshore sea ice can significantly increase in thickness. The recurrence of such events is visible in Figure 8d between 150° and 160°E, where a path of thicker sea ice extends from the coast. Similar, though less pronounced, features can be observed around 80°E, 100°E, 150°W, and 40°W. Conversely, thinner sea ice can be found downstream of landfast ice, because polynya behind them releases relatively thin ice. These thinner ice areas (see Figure 8) can expand further downstream of polynyas due to a shift from a net import of thick ice in NO_LFI to a net import of thin, newly formed ice in LFI. Ultimately, various factors (ice drift, thickness, and the presence of landfast ice) interact in a complex way, determining whether thinner or thicker ice is imported into a given region and the sign of thickness change between the two simulations.

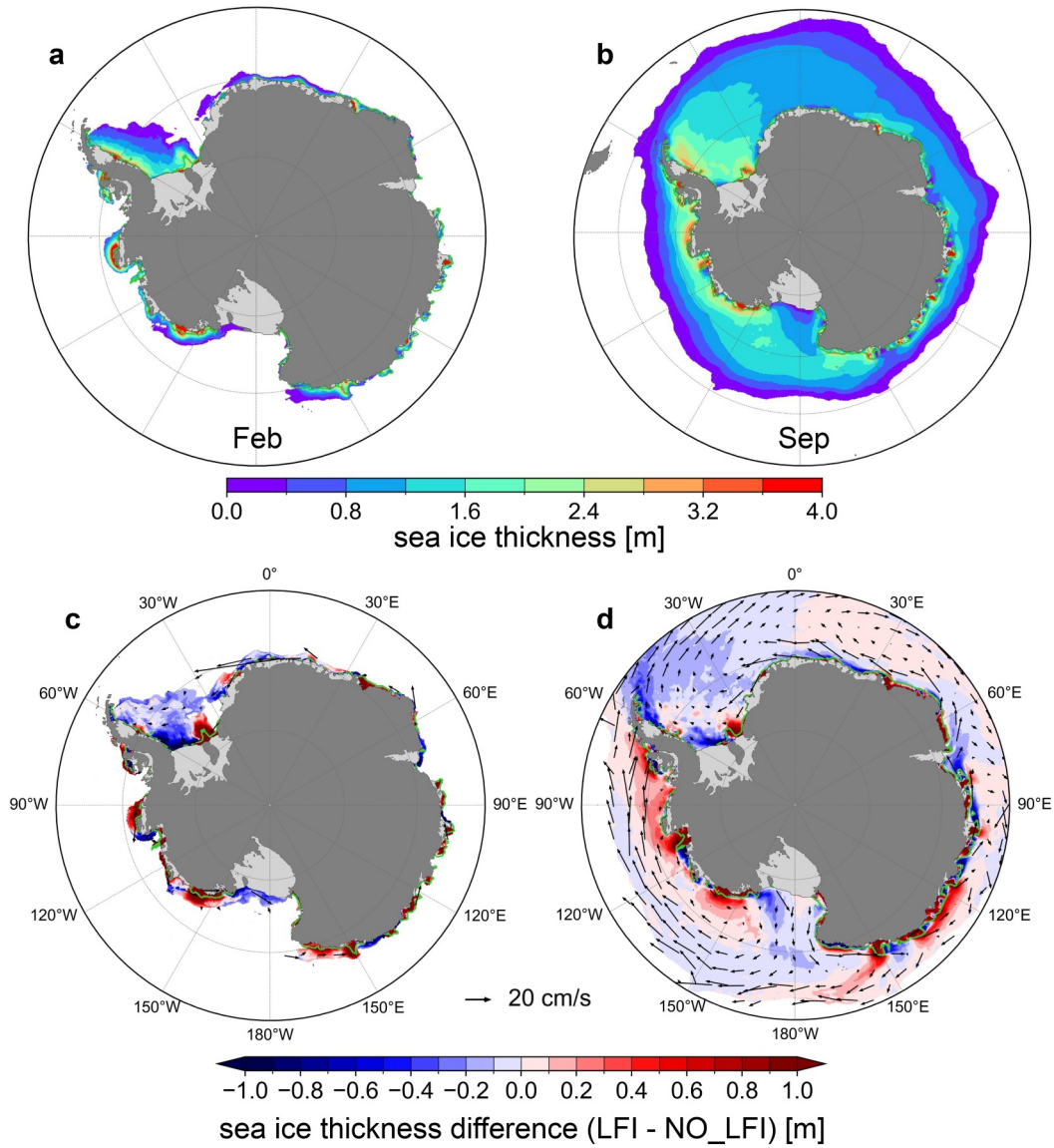


**Figure 8.** 2001–2017 mean sea ice thickness in the LFI simulation in February (a) and September (b). (c, d) Same but for the LFI minus NO_LFI difference. The green contour displays where restoring is applied more than 50% of the time. Arrows on panel (c and d) show the February and September climatology of sea ice velocity, respectively. The length of the scale arrow indicates 20 cm $s^{-1}$ drift velocity.

## 4. Discussion

Our simulations highlight a series of effects of prescribing Antarctic landfast ice on sea ice and coastal polynya dynamics. These effects confirm and extend over previous works, are physically consistent, and therefore we argue they inform on the real world effects of landfast ice.

In particular, we find the blocking effect that landfast ice exerts on its surroundings is central to the changes between the LFI and NO_LFI simulations. The landfast ice blocking effect arises because landfast ice impedes ice drift, causing thick, possibly stationary ice to accumulate upstream of the landfast ice formations, and leading to the creation of a polynya downstream. Figure 9 illustrates this for the Dibble polynya: in the NO_LFI simulation (Figure 9a), the polynya is absent as sea ice freely flows along the coast. In contrast, in the LFI simulation (Figure 9b), landfast ice creates a barrier that diverts the sea ice flow. West of the fast ice formation, katabatic winds export ice, whereas landfast ice blocks the import of thick ice from the east, resulting in the creation of a polynya. The succession of landfast ice and polynyas along the entire East Antarctic coast (central map of

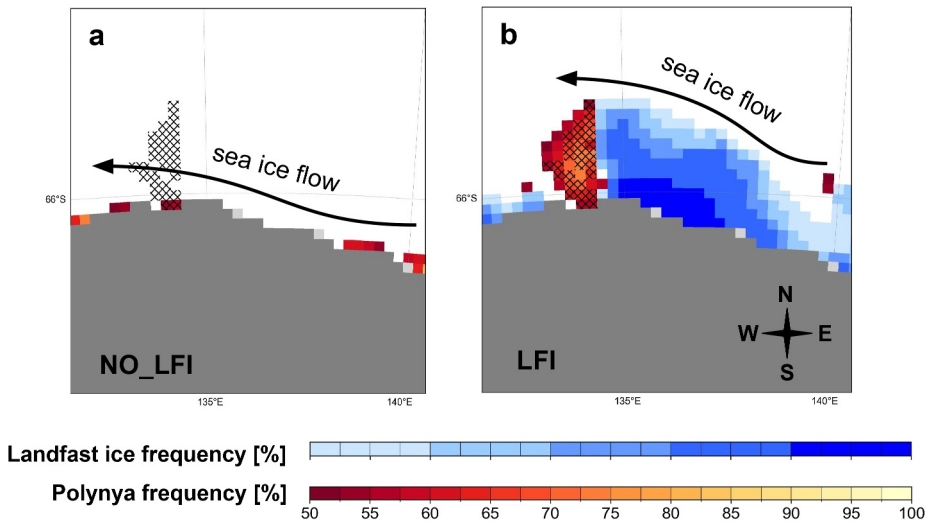


**Figure 9.** Frequency of occurrence of coastal polynya (red shading) and landfast ice (blue shading) in the Dibble polynya region, March–October 2001–2017 average, for the (a) NO_LFI and (b) LFI simulations. Hatched cells indicate the distribution of detected polynyas from an independent study (Nihashi & Ohshima, 2015).

Figure 6) suggests this mechanism works at a circumpolar scale, as hypothesized in numerous studies (e.g., Bromwich & Kurtz, 1984; Fraser et al., 2012, 2019, 2023; Huot et al., 2021; Massom et al., 1998, 2001; Morales Maqueda et al., 2004; Nihashi et al., 2023; Nihashi & Ohshima, 2015; Tamura et al., 2008, 2016; Van Achter et al., 2022).

Our simulations also highlight that landfast ice influences some polynyas (DiP, DaP, AP, VBP, MP, BaP, CP, and SP) more than others (MBP, TNBP, RISP, BeP, and RONP; definitions of abbreviations can be found in Table 2). This categorization is consistent with the initial classifications of Antarctic coastal polynyas by Massom et al. (1998), as well as the more recent classifications by Nihashi and Ohshima (2015) and Jeong et al. (2023). For the first group, polynyas are mainly influenced by landfast ice (and indirectly by grounded icebergs). For the second group, there is little or no landfast ice in the region, and other factors such as katabatic winds, a glacier tongue, an ice shelf or the continent dominate. Therefore, resolution (Jeong et al., 2023) and possibly a more accurate representation of winds (Mathiot et al., 2010) would be essential to simulate those polynyas in the second group. More generally, some polynyas remain smaller and less ice-productive compared to observational estimates. The extent to which this discrepancy is due to diagnostic uncertainty—stemming from the definition of polynyas—or to low resolution and unrealistic wind forcing remains to be determined.

Our simulations and analyses also provide the first estimate of pan-Antarctic landfast ice volume: 1,210 ± 100 $km^3$ on an annual average. This estimate benefits from the precise observational quantification of landfast ice extent and reasonably well-constrained ice thickness from our model calculation. However, without accurate knowledge of the error in landfast ice thickness—the largest source of volume uncertainty—it is challenging to precisely quantify the error in the Antarctic landfast ice volume, which future work may help.

Uncertainties in landfast ice thickness stem primarily from physical limitations in the velocity-restoring approach to represent Antarctic landfast ice. In particular, fracturing and piling processes, such as rafting and ridging, cannot, in the model, operate within the landfast ice formations. Yet, in reality, rough fast ice, suggesting the presence of pressure ridges, has been reported in some regions to contribute to large fractions of landfast ice, up to >30% of area and >50% of volume (see Giles et al., 2008; Fraser et al., 2023, and references therein). As deformed ice is much thicker than thermodynamically grown ice, the lack of deformed fast ice in the model contributes to underestimate the simulated sea ice thickness.

Another consequence of the lack of a physical basis is that velocity-restoring can only be applied when landfast ice observations are available at the circumpolar scale, namely over the last two decades. Although this lies beyond the scope of the paper, we made a preliminary attempt to use a climatological landfast ice mask, which reveals that the approach is not straightforward mainly due to difficulties of the model to simulate landfast ice

breakup. In addition, such an approach would not be credible beyond a few past or future decades, as large changes in landfast ice coverage are expected over multi-decadal time periods (Fraser et al., 2023; Massom et al., 2010). These limitations highlight the need for a physically based representation of Antarctic landfast ice. Although further efforts are needed to represent grounded icebergs in climate models, the combination of lateral drag parameterizations as proposed by Liu et al. (2022) or the dynamic iceberg-sea ice interactions as described in Hunke and Comeau (2011), with the inclusion of sea ice tensile strength (König Beatty & Holland, 2010), already offers a promising framework for simulating Antarctic landfast ice.

There are other physical issues in our simulations, in particular related to snow, and also possibly to platelet ice. The very large annual amount of snowfall in the ERA-5 reanalysis in some coastal Antarctic regions (for instance near Marguerite Bay, Bellingshausen Sea) can largely increase landfast ice thickness via snow-ice formation. However, no data are available to assess ERA-5 snowfall fields. As collecting reliable in situ snowfall rate observations near the coasts of Antarctica would be difficult, remote sensing-based snow depth estimates would definitely help progress here. The suspension and deposition effects of blowing snow on snow depth could be particularly important on fast ice given the frequency of strong winds (see Fedotov et al., 1998; Fraser et al., 2023, Section 2.2 and references therein), but are not represented in the model. Furthermore, the long-term snow accumulation capacity on ice is amplified over landfast ice, as it stays in place. At Rothera and Syowa stations, where simulated landfast ice thickness is overestimated and snow depth is fairly high, we think the lack of blowing snow in the model could be important. Given the importance of snow on sea ice, this adds significant uncertainties to simulated sea ice thickness. We suggest future modeling studies on Antarctic landfast ice consider snow and test the blowing-snow parameterization of Lecomte et al. (2015). Finally, we note that platelet ice is also not considered in our model and could also add uncertainty in sea ice thickness. Recent progress toward representing the sub-ice platelet layer has been done (Wongpan et al., 2021), but more work is necessary to have it work in three-dimensional ocean-sea ice models.

## 5. Conclusion

In this contribution, we question how a realistic representation of Antarctic landfast ice affects sea ice and coastal polynya dynamics in 1/4° ocean-sea ice model simulations. We develop and test a sea ice velocity restoring technique that restores model landfast ice to space- and time-varying Antarctic landfast ice coverage observations (Fraser et al., 2020).

We show that prescribing Antarctic landfast ice improves the realism of simulated coastal polynya and sea ice dynamics. First, it provides a precise representation of landfast ice coverage in the simulations, as intended. Moreover, restoring landfast ice location implies that landfast ice grows at the correct location and time of the year, ultimately improving its seasonal thickness cycle. Moreover, prescribing landfast ice largely improves coastal polynya dynamics, with more realistic polynya shape, larger area, and higher annual ice production. At large scales, imposing landfast ice redistributes, rather than increases, sea ice production across the continental shelf, because of compensation effects between enhanced ice growth near polynyas and large reduction in sea ice growth under landfast ice. Finally, prescribing landfast ice also maintains thick sea ice along the Antarctic coast in early summer, mitigating the low summer ice extent model bias.

Our simulations give physically based evidence that the landfast ice blocking effect is essential to many Antarctic coastal polynyas, albeit not to all of them, which confirms previous observation-based analyses (Massom et al., 1998; Nihashi & Ohshima, 2015). According to our simulations, landfast ice is particularly important to polynya activity in Dibble, Dalton, Amundsen, Vincennes Bay, Mertz, Barrier, Cape Darnley, and Shackleton Polynya regions, whereas it seems less important in Mackenzie Bay, Terra Nova Bay, Ross Ice Shelf, Ronne Ice Shelf and Bellingshausen Polynya regions.

Our simulations also provide the first pan-Antarctic quantification of Antarctic landfast ice volume for the 2001–2017 period, giving an annual average landfast ice volume of 1,210 ± 100 $km^3$, varying between a minimum of 690 ± 130 $km^3$ and a maximum of 1,730 ± 130 $km^3$. Landfast ice would therefore account for 10.6% of the annual mean Antarctic sea ice volume, whereas it represents only 3.8% of annual mean Antarctic sea ice extent.

These findings highlight the potential importance of an accurate representation of Antarctic landfast ice in large-scale ocean-sea ice model used in climate studies. Although our method is a useful first step, its application limits to when the landfast ice distribution is known, that is, over the last two decades. To investigate the more distant

past or the future, a physical representation of Antarctic landfast ice drivers would be needed. This would particularly require advancing the understanding of the anchoring of large icebergs and their dynamical interactions with sea ice. Such an endeavor should ultimately improve simulated polynyas by Earth System Models, and potentially lead to more realistic Antarctic dense shelf water production.

## Appendix A: Velocity Restoring on the Landfast Ice Mask

Here we describe the algorithm used to restore sea ice velocity to zero where and when landfast ice is observed according to Fraser et al. (2020). Landfast ice presence is specified using a space- and time-dependent mask, defined for each model grid cell and time step.

In the reference code, the drift velocity vector $u$ of the sea ice continuum is solution of the 2D linear momentum equation, which reads:

$$m\frac{\partial \mathbf{u}}{\partial t} = Air\ Drag + Water\ Drag + Coriolis\ Force + Sea\ Surface\ Tilt + Internal\ Stress \tag{A1}$$

where $m$ is the sea ice and snow mass per unit area. The SI$^3$ dynamical solver solves a discrete-in-time equation for the velocity at next time step, $\mathbf{u}^{n+1}$, given by:

$$\mathbf{u}^{n+1} = \mathbf{RHS} \cdot \Delta t + \mathbf{u}^{n} \tag{A2}$$

where RHS denotes the right-hand side of the discretized velocity equation and $\Delta t$ is the time step of the sea ice model. To calculate the sea ice stress term, the adaptive EVP (aEVP) solver of Kimmritz et al. (2016) is used. The number of pseudo-time steps in the iterative solution procedure is set to 120 in our configuration.

The velocity calculation was modified in order to restore velocity within the landfast ice mask, at each pseudo-time step. Equation A2 is modified as follows:

$$\mathbf{u}^{n+1} = \frac{\mathbf{RHS} \cdot \Delta t + \mathbf{u}^{n}}{1 + \mathbf{mask}^{n+1}/\tau} \tag{A3}$$

where $\mathbf{mask}^{n+1}$ refers to the landfast ice mask at time step $n+1$. This formulation ensures that the sea ice velocity approaches the regular physical solution (Equation A1) where the landfast ice mask is 0 and zero where the mask is 1. Different values were tested for $\tau$, the restoring strength parameter. We found $\tau = 0.01$ ensures numerical stability and convergence within 120 subcycle-iterations of the aEVP scheme. Note that in this study, the restoring formulation in Equation A3 does not correspond to the classical continuous-time relaxation $\frac{du}{dt} = -\frac{1}{T}u$, but instead to a strong sub-iteration damping, which rapidly restores velocities toward zero within the landfast ice mask.

## Appendix B: Coastal Polynya Detection Algorithm

A polynya detection algorithm was developed and used to detect coastal polynyas, operating as follows (see Figure B1). Step 1: Grid cells with sea ice thickness under a prescribed threshold value are classified as open water, and as sea ice otherwise. Step 2: Contiguous open water cells are aggregated into regions using a cross-detection method, recursively, until no more cells can be incorporated. Step 3: Open water regions are classified into three categories: the Southern Ocean is the large open water region in contact with the 30°S parallel; coastal polynyas are the open water regions in contact with Antarctica; and open-ocean polynyas are the other regions. We use thickness, not ice concentration, to identify polynyas. Using ice concentration results in very small polynyas. Indeed, because the SI$^3$ model calculates thermodynamics after dynamics, open water is rapidly sealed with ∼1 cm ice (typically within a time step).

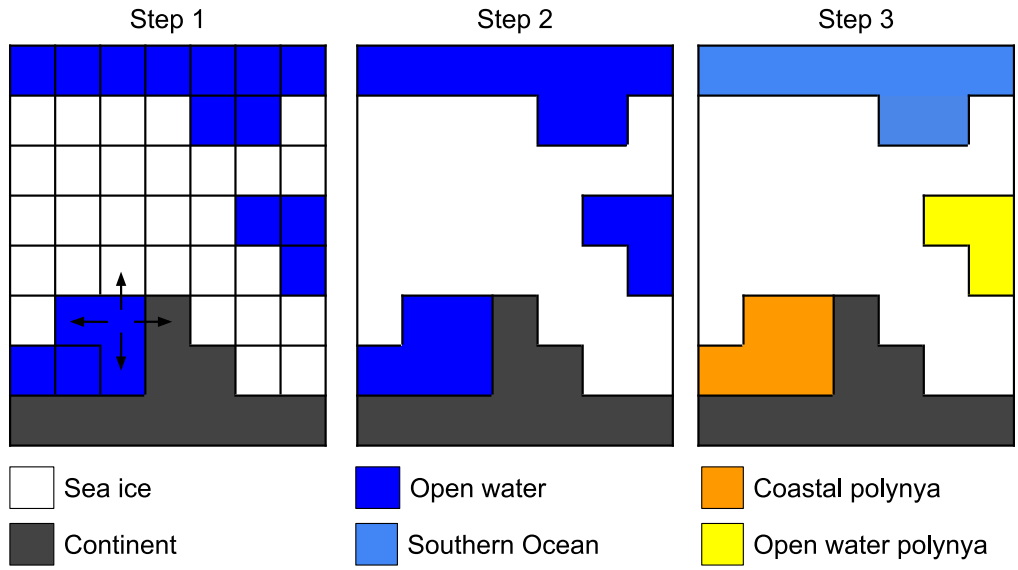


**Figure B1.** Scheme of the polynya detection algorithm steps.

## Data Availability Statement

The code of NEMO-SI$^3$ used is available from https://forge.nemo-ocean.eu/nemo/nemo/-/tree/4.2.2?ref_type=tags with the associated manual https://doi.org/10.5281/zenodo.7534900. The polynya detection algorithm is available from https://forge.uclouvain.be/NoPirlet/spot-polynya-algorithm/-/blob/main/Spot_polynyas.py?ref_type=heads. Sea ice concentration, thickness, production (in open water and bottom growth), and polynya frequency for the two simulations are available from https://doi.org/10.5281/zenodo.13985478.

**Acknowledgments**
The authors thank the two anonymous reviewers for their valuable comments and suggestions, which significantly helped improve the manuscript. We are also grateful to Q. Dalaiden for his assistance in adapting the atmospheric forcing and for many insightful discussions. We thank S. Nihashi for providing the polynya data associated with Nihashi and Ohshima (2015), and B. Richaud for proofreading the manuscript. This research was conducted within the Belgian National Fund of Scientific Research (FNRS), project LICEPOD, PDR Grant T.0079.22. Computational resources have been provided by the supercomputing facilities of the UCLouvain (CISM/UCL) and the Consortium des Equipements de Calcul Intensif en Fédération Wallonie Bruxelles (CECI), funded by the Fonds de la Recherche Scientifique—FNRS (F.R.S.–FNRS) (convention no. 2.5020.11) and by the Walloon Region. This project has received grant funding from Agence Nationale de la Recherche—France 2030 as part of the PEPR TRACCS programme under Grant ANR-22-EXTR-008, and from the Australian Government as part of the Antarctic Science Collaboration Initiative program. ADF is supported by ARC Grants FT230100234, LP170101090, LE220100103, and DP240100325, and acknowledges the generous support of the Harris Charitable Trust through the Antarctic Science Foundation. We acknowledge the use of ChatGPT (https://chat.openai.com/) to improve the writing style of a few paragraphs.

## References

Ackermann, L., Rackow, T., Himstedt, K., Gierz, P., Knorr, G., & Lohmann, G. (2024). A comprehensive Earth system model (AWI-ESM2.1) with interactive icebergs: Effects on surface and deep-ocean characteristics. *Geoscientific Model Development*, *17*(8), 3279–3301. https://doi.org/10.5194/gmd-17-3279-2024

Barnier, B., Madec, G., Penduff, T., Molines, J.-M., Treguier, A.-M., Le Sommer, J., et al. (2006). Impact of partial steps and momentum advection schemes in a global ocean circulation model at eddy-permitting resolution. *Ocean Dynamics*, *56*(5–6), 543–567. https://doi.org/10.1007/s10236-006-0082-1

Barthélemy, A., Goosse, H., Fichefet, T., & Lecomte, O. (2018). On the sensitivity of Antarctic sea ice model biases to atmospheric forcing uncertainties. *Climate Dynamics*, *51*(4), 1585–1603. https://doi.org/10.1007/s00382-017-3972-7

Bett, D. T., Holland, P. R., Naveira Garabato, A. C., Jenkins, A., Dutrieux, P., Kimura, S., & Fleming, A. (2020). The impact of the Amundsen Sea freshwater balance on ocean melting of the West Antarctic Ice Sheet. *Journal of Geophysical Research: Oceans*, *125*(9), e2020JC016305. https://doi.org/10.1029/2020JC016305

Bitz, C. M., Holland, M. M., Weaver, A. J., & Eby, M. (2001). Simulating the ice-thickness distribution in a coupled climate model. *Journal of Geophysical Research*, *106*(C2), 2441–2463. https://doi.org/10.1029/1999JC000113

Boucher, O., Servonnat, J., Albright, A. L., Aumont, O., Balkanski, Y., Bastrikov, V., et al. (2020). Presentation and evaluation of the IPSL-CM6A-LR climate model. *Journal of Advances in Modeling Earth Systems*, *12*(7), e2019MS002010. https://doi.org/10.1029/2019MS002010

Brearley, J. A., Meredith, M. P., Naveira Garabato, A. C., Venables, H. J., & Inall, M. E. (2017). Controls on turbulent mixing on the West Antarctic Peninsula shelf. *Deep Sea Research Part II: Topical Studies in Oceanography*, *139*, 18–30. https://doi.org/10.1016/j.dsr2.2017.02.011

Bromwich, D. H., & Kurtz, D. D. (1984). Katabatic wind forcing of the Terra Nova Bay polynya. *Journal of Geophysical Research*, *89*(C3), 3561–3572. https://doi.org/10.1029/JC089iC03p03561

Caton Harrison, T., Biri, S., Bracegirdle, T. J., King, J. C., Kent, E. C., Vignon, E., & Turner, J. (2022). Reanalysis representation of low-level winds in the Antarctic near-coastal region. *Weather and Climate Dynamics*, *3*(4), 1415–1437. https://doi.org/10.5194/wcd-3-1415-2022

Dammann, D. O., Eriksson, L. E. B., Mahoney, A. R., Eicken, H., & Meyer, F. J. (2019). Mapping pan-Arctic landfast sea ice stability using Sentinel-1 interferometry. *The Cryosphere*, *13*(2), 557–577. https://doi.org/10.5194/tc-13-557-2019

De Lavergne, C., Vic, C., Madec, G., Roquet, F., Waterhouse, A. F., Whalen, C. B., et al. (2020). A parameterization of local and remote tidal mixing. *Journal of Advances in Modeling Earth Systems*, *12*(5), e2020MS002065. https://doi.org/10.1029/2020MS002065

Dupont, F., Dumont, D., Lemieux, J.-F., Dumas-Lefebvre, E., & Caya, A. (2022). A probabilistic seabed–ice keel interaction model. *The Cryosphere*, *16*(5), 1963–1977. https://doi.org/10.5194/tc-16-1963-2022

Engedahl, H. (1995). Use of the flow relaxation scheme in a three-dimensional baroclinic ocean model with realistic topography. *Tellus A*, *47*(3), 365–382. https://doi.org/10.3402/tellusa.v47i3.11523

Fedotov, V. I., Cherepanov, N. V., & Tyshko, K. P. (1998). Some features of the growth, structure and metamorphism of East Antarctic landfast sea ice. In *Antarctic sea ice: Physical processes, interactions and variability* (pp. 343–354). American Geophysical Union (AGU). https://doi.org/10.1029/AR074p0343

Fichefet, T., & Maqueda, M. A. M. (1999). Modelling the influence of snow accumulation and snow-ice formation on the seasonal cycle of the Antarctic sea-ice cover. *Climate Dynamics*, *15*(4), 251–268. https://doi.org/10.1007/s003820050280

Flather, R. A. (1994). A storm surge prediction model for the northern Bay of Bengal with application to the cyclone disaster in April 1991. *Journal of Physical Oceanography*, *24*(1), 172–190. https://doi.org/10.1175/1520-0485(1994)024⟨0172:ASSPMF⟩2.0.CO;2

Fraser, A. D., Massom, R. A., Handcock, M. S., Reid, P., Ohshima, K. I., Raphael, M. N., et al. (2021). Eighteen-year record of circum-Antarctic landfast sea ice distribution allows detailed baseline characterisation, reveals trends and variability. *The Cryosphere*, *15*(11), 5061–5077. https://doi.org/10.5194/tc-15-5061-2021

Fraser, A. D., Massom, R. A., Michael, K. J., Galton-Fenzi, B. K., & Lieser, J. L. (2012). East Antarctic landfast sea ice distribution and variability, 2000–08. *Journal of Climate*, *25*(4), 1137–1156. https://doi.org/10.1175/JCLI-D-10-05032.1

Fraser, A. D., Massom, R. A., Ohshima, K. I., Willmes, S., Kappes, P. J., Cartwright, J., & Porter-Smith, R. (2020). High-resolution mapping of circum-Antarctic landfast sea ice distribution, 2000–2018. *Earth System Science Data*, *12*(4), 2987–2999. https://doi.org/10.5194/essd-12-2987-2020

Fraser, A. D., Ohshima, K. I., Nihashi, S., Massom, R. A., Tamura, T., Nakata, K., et al. (2019). Landfast ice controls on sea-ice production in the Cape Darnley Polynya: A case study. *Remote Sensing of Environment*, *233*, 111315. https://doi.org/10.1016/j.rse.2019.111315

Fraser, A. D., Wongpan, P., Langhorne, P. J., Klekociuk, A. R., Kusahara, K., Lannuzel, D., et al. (2023). Antarctic landfast sea ice: A review of its physics, biogeochemistry and ecology. *Reviews of Geophysics*, *61*(2), e2022RG000770. https://doi.org/10.1029/2022RG000770

Gent, P. R., & Mcwilliams, J. C. (1990). Isopycnal mixing in ocean circulation models. *Journal of Physical Oceanography*, *20*(1), 150–155. https://doi.org/10.1175/1520-0485(1990)020⟨0150:IMIOCM⟩2.0.CO;2

Giles, K. A., Laxon, S. W., & Worby, A. P. (2008). Antarctic sea ice elevation from satellite radar altimetry. *Geophysical Research Letters*, *35*(3), 2007GL031572. https://doi.org/10.1029/2007GL031572

Gordon, A. L., Visbeck, M., & Huber, B. (2001). Export of Weddell Sea deep and bottom water. *Journal of Geophysical Research*, *106*(C5), 9005–9017. https://doi.org/10.1029/2000JC000281

Griffies, S. M., Biastoch, A., Böning, C., Bryan, F., Danabasoglu, G., Chassignet, E. P., et al. (2009). Coordinated Ocean-ice reference experiments (COREs). *Ocean Modelling*, *26*(1–2), 1–46. https://doi.org/10.1016/j.ocemod.2008.08.007

Grotti, M., Soggia, F., Ianni, C., & Frache, R. (2005). Trace metals distributions in coastal sea ice of Terra Nova Bay, Ross Sea, Antarctica. *Antarctic Science*, *17*(2), 289–300. https://doi.org/10.1017/S0954102005002695

Hersbach, H., Bell, B., Berrisford, P., Hirahara, S., Horányi, A., Muñoz-Sabater, J., et al. (2020). The ERA5 global reanalysis. *Quarterly Journal of the Royal Meteorological Society*, *146*(730), 1999–2049. https://doi.org/10.1002/qj.3803

Heuzé, C. (2021). Antarctic bottom water and North Atlantic deep water in CMIP6 models. *Ocean Science*, *17*(1), 59–90. https://doi.org/10.5194/os-17-59-2021

Hunke, E. C., & Comeau, D. (2011). Sea ice and iceberg dynamic interaction. *Journal of Geophysical Research*, *116*(C5), C05008. https://doi.org/10.1029/2010JC006588

Huot, P.-V., Kittel, C., Fichefet, T., Jourdain, N. C., Sterlin, J., & Fettweis, X. (2021). Effects of the atmospheric forcing resolution on simulated sea ice and polynyas off Adélie Land, East Antarctica. *Ocean Modelling*, *168*, 101901. https://doi.org/10.1016/j.ocemod.2021.101901

Inall, M. E., Brearley, J. A., Henley, S. F., Fraser, A. D., & Reed, S. (2022). Landfast ice controls on turbulence in Antarctic coastal seas. *Journal of Geophysical Research: Oceans*, *127*(1), e2021JC017963. https://doi.org/10.1029/2021JC017963

Jeong, H., Turner, A. K., Roberts, A. F., Veneziani, M., Price, S. F., Asay-Davis, X. S., et al. (2023). Southern Ocean polynyas and dense water formation in a high-resolution, coupled Earth system model. *The Cryosphere*, *17*(7), 2681–2700. https://doi.org/10.5194/tc-17-2681-2023

Kimmritz, M., Danilov, S., & Losch, M. (2016). The adaptive EVP method for solving the sea ice momentum equation. *Ocean Modelling*, *101*, 59–67. https://doi.org/10.1016/j.ocemod.2016.03.004

Kittel, C., Amory, C., Agosta, C., Jourdain, N. C., Hofer, S., Delhasse, A., et al. (2021). Diverging future surface mass balance between the Antarctic ice shelves and grounded ice sheet. *The Cryosphere*, *15*(3), 1215–1236. https://doi.org/10.5194/tc-15-1215-2021

König Beatty, C., & Holland, D. M. (2010). Modeling landfast sea ice by adding tensile strength. *Journal of Physical Oceanography*, *40*(1), 185–198. https://doi.org/10.1175/2009JPO4105.1

Kusahara, K., Hasumi, H., & Tamura, T. (2010). Modeling sea ice production and dense shelf water formation in coastal polynyas around East Antarctica. *Journal of Geophysical Research*, *115*(C10), 2010JC006133. https://doi.org/10.1029/2010JC006133

Kusahara, K., Williams, G. D., Tamura, T., Massom, R., & Hasumi, H. (2017). Dense shelf water spreading from Antarctic coastal polynyas to the deep Southern Ocean: A regional circumpolar model study. *Journal of Geophysical Research: Oceans*, *122*(8), 6238–6253. https://doi.org/10.1002/2017JC012911

Langhorne, P. J., Haas, C., Price, D., Rack, W., Leonard, G. H., Brett, G. M., & Urbini, S. (2023). Fast ice thickness distribution in the western Ross Sea in late spring. *Journal of Geophysical Research: Oceans*, *128*(2), e2022JC019459. https://doi.org/10.1029/2022JC019459

Large, W., & Yeager, S. (2004). *Diurnal to decadal global forcing for ocean and sea-ice models: The data sets and flux climatologies* (Technical Report). UCAR/NCAR. https://doi.org/10.5065/D6KK98Q6

Lecomte, O., Fichefet, T., Flocco, D., Schroeder, D., & Vancoppenolle, M. (2015). Interactions between wind-blown snow redistribution and melt ponds in a coupled ocean–sea ice model. *Ocean Modelling*, *87*, 67–80. https://doi.org/10.1016/j.ocemod.2014.12.003

Lemieux, J.-F., Dupont, F., Blain, P., Roy, F., Smith, G. C., & Flato, G. M. (2016). Improving the simulation of landfast ice by combining tensile strength and a parameterization for grounded ridges. *Journal of Geophysical Research: Oceans*, *121*(10), 7354–7368. https://doi.org/10.1002/2016JC012006

Lemieux, J.-F., Tremblay, L. B., Dupont, F., Plante, M., Smith, G. C., & Dumont, D. (2015). A basal stress parameterization for modeling landfast ice. *Journal of Geophysical Research: Oceans*, *120*(4), 3157–3173. https://doi.org/10.1002/2014JC010678

Lin, X., Massonnet, F., Fichefet, T., & Vancoppenolle, M. (2023). Impact of atmospheric forcing uncertainties on Arctic and Antarctic sea ice simulations in CMIP6 OMIP models. *The Cryosphere*, *17*(5), 1935–1965. https://doi.org/10.5194/tc-17-1935-2023

Lipscomb, W. H. (2001). Remapping the thickness distribution in sea ice models. *Journal of Geophysical Research*, *106*(C7), 13989–14000. https://doi.org/10.1029/2000JC000518

Liu, Y., Losch, M., Hutter, N., & Mu, L. (2022). A new parameterization of coastal drag to simulate landfast ice in deep marginal seas in the Arctic. *Journal of Geophysical Research: Oceans*, *127*(6), e2022JC018413. https://doi.org/10.1029/2022JC018413

Locarnini, M., Mishonov, A., Baranova, O., Boyer, T., Zweng, M., Garcia, H., et al. (2018). *World Ocean Atlas 2018, Volume 1: Temperature* (Report). Archimer. Retrieved from https://archimer.ifremer.fr/doc/00651/76338/

Madec, G., Bell, M., Blaker, A., Bricaud, C., Bruciaferri, D., Castrillo, M., et al. (2023). NEMO ocean engine reference manual [Dataset]. *Zenodo*. https://doi.org/10.5281/ZENODO.1464816

Mahoney, A. R., Eicken, H., Gaylord, A. G., & Gens, R. (2014). Landfast sea ice extent in the Chukchi and Beaufort Seas: The annual cycle and decadal variability. *Cold Regions Science and Technology*, *103*, 41–56. https://doi.org/10.1016/j.coldregions.2014.03.003

Massom, R. A., Giles, A. B., Fricker, H. A., Warner, R. C., Legrésy, B., Hyland, G., et al. (2010). Examining the interaction between multi-year landfast sea ice and the Mertz Glacier Tongue, East Antarctica: Another factor in ice sheet stability? *Journal of Geophysical Research*, *115*(C12), 2009JC006083. https://doi.org/10.1029/2009JC006083

Massom, R. A., Harris, P., Michael, K. J., & Potter, M. (1998). The distribution and formative processes of latent-heat polynyas in East Antarctica. *Annals of Glaciology*, *27*, 420–426. https://doi.org/10.3189/1998AoG27-1-420-426

Massom, R. A., Hill, K. L., Lytle, V. I., Worby, A. P., Paget, M., & Allison, I. (2001). Effects of regional fast-ice and iceberg distributions on the behaviour of the Mertz Glacier polynya, East Antarctica. *Annals of Glaciology*, *33*, 391–398. https://doi.org/10.3189/172756401781818518

Massom, R. A., Scambos, T. A., Bennetts, L. G., Reid, P., Squire, V. A., & Stammerjohn, S. E. (2018). Antarctic ice shelf disintegration triggered by sea ice loss and ocean swell. *Nature*, *558*(7710), 383–389. https://doi.org/10.1038/s41586-018-0212-1

Massom, R. A., & Stammerjohn, S. E. (2010). Antarctic sea ice change and variability – Physical and ecological implications. *Polar Science*, *4*(2), 149–186. https://doi.org/10.1016/j.polar.2010.05.001

Mathiot, P., Barnier, B., Gallée, H., Molines, J. M., Sommer, J. L., Juza, M., & Penduff, T. (2010). Introducing katabatic winds in global ERA40 fields to simulate their impacts on the Southern Ocean and sea-ice. *Ocean Modelling*, *35*(3), 146–160. https://doi.org/10.1016/j.ocemod.2010.07.001

Mathiot, P., Jenkins, A., Harris, C., & Madec, G. (2017). Explicit representation and parametrised impacts of under ice shelf seas in the *z** coordinate ocean model NEMO 3.6. *Geoscientific Model Development*, *10*(7), 2849–2874. https://doi.org/10.5194/gmd-10-2849-2017

Mathiot, P., & Jourdain, N. C. (2023). Southern Ocean warming and Antarctic ice shelf melting in conditions plausible by late 23rd century in a high-end scenario. *Ocean Science*, *19*(6), 1595–1615. https://doi.org/10.5194/os-19-1595-2023

Meiners, K. M., Vancoppenolle, M., Carnat, G., Castellani, G., Delille, B., Delille, D., et al. (2018). Chlorophyll-*a* in Antarctic landfast sea ice: A first synthesis of historical ice core data. *Journal of Geophysical Research: Oceans*, *123*(11), 8444–8459. https://doi.org/10.1029/2018JC014245

Mohrmann, M., Heuzé, C., & Swart, S. (2021). Southern Ocean polynyas in CMIP6 models. *The Cryosphere*, *15*(9), 4281–4313. https://doi.org/10.5194/tc-2021-23

Morales Maqueda, M. A., Willmott, A. J., & Biggs, N. R. T. (2004). Polynya dynamics: A review of observations and modeling. *Reviews of Geophysics*, *42*(1), 2002RG000116. https://doi.org/10.1029/2002RG000116

Nakamura, K., Wakabayashi, H., Uto, S., Ushio, S., & Nishio, F. (2009). Observation of sea-ice thickness using ENVISAT data from Lützow-Holm Bay, East Antarctica. *IEEE Geoscience and Remote Sensing Letters*, *6*(2), 277–281. https://doi.org/10.1109/LGRS.2008.2011061

Nakata, K., Ohshima, K. I., & Nihashi, S. (2021). Mapping of active frazil for Antarctic coastal polynyas, with an estimation of sea-ice production. *Geophysical Research Letters*, *48*(6), e2020GL091353. https://doi.org/10.1029/2020GL091353

Nihashi, S., & Ohshima, K. I. (2015). Circumpolar mapping of Antarctic coastal polynyas and landfast sea ice: Relationship and variability. *Journal of Climate*, *28*(9), 3650–3670. https://doi.org/10.1175/JCLI-D-14-00369.1

Nihashi, S., Ohshima, K. I., & Tamura, T. (2023). Reconstruct the AMSR-E/2 thin ice thickness algorithm to create a long-term time series of sea-ice production in Antarctic coastal polynyas. *Polar Science*, *39*, 100978. https://doi.org/10.1016/j.polar.2023.100978

Ohshima, K. I., Fukamachi, Y., Ito, M., Nakata, K., Simizu, D., Ono, K., et al. (2022). Dominant frazil ice production in the Cape Darnley polynya leading to Antarctic Bottom Water formation. *Science Advances*, *8*(42), eadc9174. https://doi.org/10.1126/sciadv.adc9174

Ohshima, K. I., Fukamachi, Y., Williams, G. D., Nihashi, S., Roquet, F., Kitade, Y., et al. (2013). Antarctic Bottom Water production by intense sea-ice formation in the Cape Darnley polynya. *Nature Geoscience*, *6*(3), 235–240. https://doi.org/10.1038/ngeo1738

Ohshima, K. I., Nihashi, S., & Iwamoto, K. (2016). Global view of sea-ice production in polynyas and its linkage to dense/bottom water formation. *Geoscience Letters*, *3*(1), 13. https://doi.org/10.1186/s40562-016-0045-4

Prather, M. J. (1986). Numerical advection by conservation of second-order moments. *Journal of Geophysical Research*, *91*(D6), 6671–6681. https://doi.org/10.1029/JD091iD06p06671

Rintoul, S. R., & Bullister, J. L. (1999). A late winter hydrographic section from Tasmania to Antarctica. *Deep Sea Research Part I: Oceanographic Research Papers*, *46*(8), 1417–1454. https://doi.org/10.1016/S0967-0637(99)00013-8

Roquet, F., Madec, G., McDougall, T. J., & Barker, P. M. (2015). Accurate polynomial expressions for the density and specific volume of seawater using the TEOS-10 standard. *Ocean Modelling*, *90*, 29–43. https://doi.org/10.1016/j.ocemod.2015.04.002

Rousset, C., Vancoppenolle, M., Madec, G., Fichefet, T., Flavoni, S., Barthélemy, A., et al. (2015). The Louvain-La-Neuve sea ice model LIM3.6: Global and regional capabilities. *Geoscientific Model Development*, *8*(10), 2991–3005. https://doi.org/10.5194/gmd-8-2991-2015

Sterlin, J., Orval, T., Lemieux, J.-F., Rousset, C., Fichefet, T., Massonnet, F., & Raulier, J. (2024). Influence of the representation of landfast ice on the simulation of the Arctic sea ice and Arctic Ocean halocline. *Ocean Dynamics*, *74*(5), 407–437. https://doi.org/10.1007/s10236-024-01611-0

Storkey, D., Blaker, A. T., Mathiot, P., Megann, A., Aksenov, Y., Blockley, E. W., et al. (2018). UK Global Ocean GO6 and GO7: A traceable hierarchy of model resolutions. *Geoscientific Model Development*, *11*(8), 3187–3213. https://doi.org/10.5194/gmd-11-3187-2018

Tamura, T., Ohshima, K. I., Fraser, A. D., & Williams, G. D. (2016). Sea ice production variability in Antarctic coastal polynyas. *Journal of Geophysical Research: Oceans*, *121*(5), 2967–2979. https://doi.org/10.1002/2015JC011537

Tamura, T., Ohshima, K. I., Enomoto, H., Tateyama, K., Muto, A., Ushio, S., & Massom, R. A. (2006). Estimation of thin sea-ice thickness from NOAA AVHRR data in a polynya off the Wilkes Land coast, East Antarctica. *Annals of Glaciology*, *44*, 269–274. https://doi.org/10.3189/172756406781811745

Tamura, T., Ohshima, K. I., & Nihashi, S. (2008). Mapping of sea ice production for Antarctic coastal polynyas. *Geophysical Research Letters*, *35*(7), 2007GL032903. https://doi.org/10.1029/2007GL032903

Van Achter, G., Fichefet, T., Goosse, H., Pelletier, C., Sterlin, J., Huot, P.-V., et al. (2022). Modelling landfast sea ice and its influence on ocean–ice interactions in the area of the Totten Glacier, East Antarctica. *Ocean Modelling*, *169*, 101920. https://doi.org/10.1016/j.ocemod.2021.101920

Vancoppenolle, M., Fichefet, T., Goosse, H., Bouillon, S., Madec, G., & Maqueda, M. A. M. (2009). Simulating the mass balance and salinity of Arctic and Antarctic sea ice. 1. Model description and validation. *Ocean Modelling*, *27*(1–2), 33–53. https://doi.org/10.1016/j.ocemod.2008.10.005

Vancoppenolle, M., Rousset, C., Blockley, E., Aksenov, Y., Feltham, D., Fichefet, T., et al. (2023). SI3, the NEMO sea ice engine [Dataset]. *Zenodo*. https://doi.org/10.5281/zenodo.7534900

Williams, G. D., Herraiz-Borreguero, L., Roquet, F., Tamura, T., Ohshima, K. I., Fukamachi, Y., et al. (2016). The suppression of Antarctic bottom water formation by melting ice shelves in Prydz Bay. *Nature Communications*, *7*(1), 12577. https://doi.org/10.1038/ncomms12577

Wongpan, P., Meiners, K. M., Vancoppenolle, M., Fraser, A. D., Moreau, S., Saenz, B. T., et al. (2024). Gross primary production of Antarctic landfast sea ice: A model-based estimate. *Journal of Geophysical Research: Oceans*, *129*(10), e2024JC021348. https://doi.org/10.1029/2024JC021348

Wongpan, P., Vancoppenolle, M., Langhorne, P. J., Smith, I. J., Madec, G., Gough, A. J., et al. (2021). Sub-ice platelet layer physics: Insights from a mushy-layer sea ice model. *Journal of Geophysical Research: Oceans*, *126*(6), e2019JC015918. https://doi.org/10.1029/2019JC015918

Zalesak, S. T. (2012). The design of flux-corrected transport (FCT) algorithms for structured grids. In D. Kuzmin, R. Löhner, & S. Turek (Eds.), *Flux-corrected transport: Principles, algorithms, and applications* (pp. 23–65). Springer Netherlands. https://doi.org/10.1007/978-94-007-4038-9_2

Zuo, H., Balmaseda, M. A., Tietsche, S., Mogensen, K., & Mayer, M. (2019). The ECMWF operational ensemble reanalysis–analysis system for ocean and sea ice: A description of the system and assessment. *Ocean Science*, *15*(3), 779–808. https://doi.org/10.5194/os-15-779-2019

Zweng, M., Reagan, J., Seidov, D., Boyer, T., Locarnini, M., Garcia, H., et al. (2019). *World ocean atlas 2018, volume 2: Salinity* (Vol. 61). NOAA Atlas NESDIS.